Faculty of Science and Engineering
Department of Exploration Geophysics

Frequency-domain fibre optic pressure sensors for Geophysical applications

Vladimir Roumenov Bossilkov

This thesis is presented for the Degree of
Master of Philosophy (Geophysics)
of
Curtin University

June 2015

Declaration

To the best of my knowledge and belief this thesis contains no material previously published by any other person except where due acknowledgement has been made.

This thesis contains no material which has been accepted for the award of any other degree or diploma in any university.

Signature

Date

Dedication

This thesis is dedicated to my late cat, Pooh, who perished the morning of the formal enrolment as Master's by Research student.

Abstract

This Master's thesis seeks to explore an alternative approach to fibre-optic strain interrogation. Instead of looking at the conventional phase delays created by fibre strain, frequency-domain shifts are considerer here. Frequency-domain shift sensing has been made possible by relatively recent advances in modern optical physics, and this thesis seeks to illustrate that future pressure or strain sensors could be innovated by incorporating designs discussed here. A number of methods for frequency-domain sensing are presented and compared with the intention of designing a hydrophone for seismic acquisition. Of the methods compared, the Long Period Fibre Grating, investigated thoroughly by this thesis, shows the most promise by exhibiting theoretically high strain sensitivity. This grating is modelled in detail to ascertain its viability as a hydrophone instrument, with a goal to utilise tightly bendable plastic fibres to create highly compact compliant mandrels. Aside from hydrophones, down-hole pressure sensors are also considered, and methods considered are found to be very viable, as large dynamic range becomes more important than strain sensitivity. Through uncertainty analysis, Long Period Fibre Grating sensors were found to be too difficult to manufacture as hydrophones due to the high sensitivity requirements. On the other hand, due to the frequency-domain sensors having inherently broad dynamic range, down-hole instruments can be designed based on a number of the considered frequency-domain methods.

Contents

1 Thesis Introduction **4**

2 Background **6**

2.1 Introduction 6

2.2 Review of Processes 6

2.2.1 Review of Brillouin Scattering 6

2.2.2 Review of Raman Scattering 7

2.2.3 Review of Rayleigh Scattering 8

2.2.4 Review of White light based Fiber-Optic Extrinsic Fabry-Perot Interferometer 11

2.2.5 Review of Long Period Fibre Grating 11

2.3 Discussion of Benefits and Limitations 14

2.3.1 Brillouin/Raman Scattering 14

2.3.2 Rayleigh Scattering 15

2.3.3 Long Period Fibre Grating 15

2.4 Sensitivity Summary / Conclusion 16

3 Long Period Fibre Grating Theory **17**

3.1 Description of core and cladding modes and Grating Characteristics 17

3.2 Strain sensitivity of a Long Period Fibre Grating 23

3.3 Conclusion 25

4 Long Period Fibre Grating Solution Implementation **26**

4.1 Turning Point Solutions 26

4.2 Spectral Characteristics 26

4.3 Conclusion 29

5 Mandrel Theory **31**

5.1 Introduction 31

5.2 Mandrel Sensitivity Theory 31

5.3 Design Specifications 36

5.4 Predicted Operating Specifications 37

5.4.1 Air-backed Mandrel 38

5.5 Conclusion 38

6 Proposed System Design **40**
6.1 Introduction . . . 40
6.2 Signal Spectrum . . . 40
6.3 Source Spectrum . . . 42
6.4 Heterodyne Signal to Noise Ratio . . . 43
6.5 Proposed Arrangement . . . 43
6.6 Conclusion . . . 44

7 Uncertainty Analysis **45**
7.1 Forward Uncertainty Propagation Analysis . . . 45
7.1.1 Introduction . . . 45
7.1.2 Uncertainty in calculating LPFG coupling and sensitivity . . . 46
7.1.3 Uncertainty in calculating Mandrel Sensitivity . . . 48
7.2 Required Tolerance values for reproducible LPFG . . . 49
7.2.1 Introduction . . . 49
7.2.2 Derivation of Uncertainties . . . 50
7.3 Conclusion . . . 51

8 Down-Hole Implementation and Future Work **53**
8.1 Down-Hole Implementation . . . 53
8.2 Future Work . . . 55
8.2.1 Down-hole . . . 55
8.2.2 Hydrophones . . . 55

9 Conclusions **57**

A LPFG in fibres with refractive index and diameter modulation **61**

Chapter 1

Thesis Introduction

Fibre optic pressure sensors, in particular hydrophones, have revolved around the concept of sensing phase differences in a laser driven signal/reference pair since their inception almost 40 years ago (Shajenko et al., 1978), primarily due to the fact that interferometric techniques which measure phase change have good sensitivity characteristics (Yu, 2002, p. 425). The purpose of this thesis is to examine whether alternative instrument designs of strain sensors for the purpose of seismic acquisition could be conceivably built. Specifically, this thesis looks to present alternative fibre strain/pressure sensing methods; in particular methods where strain applied on a fibre causes spectral shifts in an observed spectrum. Discussion extends to the design of a compact and cost effective strain sensor, ending in a proposed design based on the process best fit for seismic acquisition as well as some applications of interest to Curtin University's Department of Exploration Targeting, namely Down-Hole pressure sensing. There is a broad range of applications in the Geo-sciences for such sensors, including but not limited to long-term Down-Hole monitoring, pressure sensing while drilling, and hydrophone instruments. The outcomes of this thesis could be made applicable to pressure sensors for the Shuttle and Coiled Tubing Rigs, being developed by the Deep Exploration Technologies CRC (DET CRC).

It is the specific goal in this thesis to look at mechanisms associated with optical fibres that create frequency-domain shifts in the detected spectrum. Spectral analysis has come a long way in the last two decades, with progress in photodetectors (Wood, 1994), frequency combs for frequency measurement (Ye and Cundiff, 2005), absorption line-shape measurements (Truong et al., 2012), super-continuum generation (Dudley and Taylor, 2010, Chapter 8) for generating spectrally broad signals, and many other tools that can contribute to making better optical sensors. Whilst Optics has come a long way, few Geophysical optical instruments have adopted modern concepts in their functionality. This is the driving motivation for this research into ways to utilise frequency-domain shifts that would be interrogated by methods enabled by modern optics, for the purpose of creating a pressure sensing instrument that could be applied to a variety of Geophysical applications, like seismic acquisition and down-hole pressure sensing while drilling.

This thesis will firstly compare a number of intrinsic and extrinsic methods for generating frequency-domain shifts from fibre strain; then design a fibre wound mandrel pressure sensor based on the most sensitive mechanism, in order to create a compact sensor; and lastly, analyse whether such a sensor would be reproducibly constructible through means of uncertainty analysis. Among

the various ways to utilise frequency domain shifts, several designs stand out as particularly useful. These are the Tapered-fibre Rayleigh backscatter, the diaphragm extrinsic Fabry-Perot cavity, and the Long Period Fibre grating.

These three designs have a common feature, that creates predictable interference patterns observable in the frequency domain, where this interference pattern moves significantly with strains on the fibre or changes in pressure. The detection of these shifts is best done using cross-correlation algorithms or heterodyne arrangements, and each have their strengths and weaknesses. A heterodyne, first developed by Forrester (1961), is a method of mixing two signals enabling a bandpass filter to easily extract the frequency difference between them. Developments by Wood (1994) in high speed photodetectors, mean that working in the optical spectrum was much easier. With more recent advances in spectral shift detection with an optical heterodyne implementations, laser frequency shifts at resolutions as low as 60 Hz can be recovered from spectra (Lu et al., 2015), though to extend these ideas would required experimentation.

Of the frequency-domain methods looked at, Long Period Fibre Gratings have been mathematically modelled accurately by Erdogan (1997a), are theoretically promising, and have had little in the way of development as commercial strain or pressure sensors. Though at least one design has been proposed by (Wang et al., 2009) where the phase-domain characteristics of a bent Long Period Fibre Grating is utilised as a hydrophone, it is poorly written and details of strain sensitivity and resolution are absent. Due to the absence of instrument designs with these gratings, a major goal of this thesis is to detailed evaluation of a Long Period Fibre Grating (LPFG) based sensor and how it could be utilised with an optical heterodyne, even though these gratings produce a transmission absorption line and are not actually a backscattering mechanism.

Shy of constructing a practical LPFG, this thesis delves into implementation with a compliant mandrel and theoretical evaluation of sensitivity, culminating in a system design. Since the theory is well established it was possible to conduct careful uncertainty propagation of the geometric variables defining the optical fibre, in order to determine whether highly sensitive LPFGs capable of competing with existing sensors are reliably manufacturable. This analysis goes on to show that, even for a very simple case of an unwound fibre, very precisely manufactured optical fibre is required to achieve the high sensitivities and narrow absorption lines which are needed for an effective hydrophone design. However a Down-Hole monitoring pressure sensor is presently more viable, since sensitivity requirements are lower.

The bulk of this thesis covers the discussion of the Long Period Fibre Grating (LPFG), most of which was accomplished through mathematical modelling using the Wolfram Mathematica software. These gratings in particular showed great promise when considered in theory, due to potentially very high strain sensitivities. Solving for the absorption and strain characteristics is a large part of the work (covered in LPFGeval.nb), and the code used in solving the gratings (LPFGcalcLoop.nb) is attached with this thesis. Moreover, a simple implementation of a LPFG wound on compliant mandrel is illustrated (MandrelEval.nb). Lastly, code for the uncertainty propagation of LPFGs and mandrels is also attached (LPFGuncertainty.nb).

Chapter 2

Background

2.1 Introduction

Fibre optic sensors can be split up into two very broad groups based on their principle of function. The most popular principle is to use interferometric sensors such as Michelson or Fabry-Perot interferometers to utilise light's phase differences to measure the strain on an optic fibre. Meanwhile this thesis focuses on the other main principle, namely wavelength shifts to measure strain, otherwise known as Optical Frequency Domain Reflectometry (OFDR). Certain interferometric designs can be altered to utilise OFDR, and are discussed in this chapter.

There main of advantages to OFDR sensors:

- Sensors are immune to power fluctuations of the source since relative amplitudes are not important.
- Wavelength differences can be measured with high resolution with a heterodyne.
- Dynamic range is limited by the bandwidth of the intermediate filter of a heterodyne, which can be changed on-the-fly.

Summarising all the different implementations is a difficult task. Some ideas using sensing crystal strains, or even quantum mechanical strain measurements are not be covered here as the focus is on making a fibre-optic sensor. This chapter reviews a set of fibre optic based OFDR options, and goes on to discuss the practicality of using any given fibre based option.

2.2 Review of Processes

2.2.1 Review of Brillouin Scattering

Brillouin backscattering is the scattering of a photon from density (or induced refractive index) changes. This is known as photon-phonon scattering, where a phonon is a quantum mechanical pseudo-particle, describing a density wave. Brillouin backscattering has seen industrial applications, monitoring strain in structures (Measures, 2001).

A mathematical description of Brillouin backscattering frequency down-shift (ω_B) is as follows (Mizuno et al., 2012):

$$\omega_B = \frac{2n_{\text{co}}v_A}{\lambda} \tag{2.1}$$

Where n_{co} is the refractive index of the fibre core, v_A is the acoustic velocity in the fibre (which depends on strain) and λ is the wavelength of the incident light.

The Brillouin frequency is linearly related to strain and temperature by the following equations (Brown et al., 2005):

$$\omega_B\left(T\right) = C_T\ T + \omega_{B0} \tag{2.2}$$

$$\omega_B\left(\epsilon\right) = C_\epsilon\ \epsilon + \omega_{B0} \tag{2.3}$$

The typical value of C_ϵ in silicon is about 0.058 MHz/$\mu\epsilon$, or 6.35×10^{-4} nm/mϵ at a laser wavelength of about 1500 nm. This is a very poor sensitivity compared to others discussed in this chapter. However the line-width of Brillouin scattering is very narrow (Boyd, 2008, Chapter 9), on the order of 10 MHz (or about 0.1 pm centred on 1500 nm), meaning that measurements made using Brillouin scattering will be finely resolved with a heterodyne.

In a paper by Zhu et al. (2010), recovery of a Brillouin scattered signal is demonstrated using a heterodyne to compare scattered wavelength-shifted coded signal, with an un-shifted coded reference signal. This allows for real-time Brillouin measurements to be made on a 60 km long cable, without a requirement for a high power pump (the Local Oscillator, usually the main stable laser of the system). While this sort of system could be applied to some industrial applications where the strains exerted on the cable are relatively large, the system is unsuitable for detection of small changes in strain that would occur in a cable used for seismic acquisition. For this reason Brillouin backscattering could be implemented in sensors for Down-Hole depth sensing, or strain monitoring to detect leaks in cemented CO_2 trap drill wells.

Brillouin scattering sensitivity and line-width vary with different materials, as exhibited by Mizuno et al. (2010). They illustrate half the sensitivity of plain silicon fibre but a narrowing of the line-width by 6 times, through the use of a tellurite optical fibre.

2.2.2 Review of Raman Scattering

Raman backscattering is very low amplitude light that is produced by inelastic scattering from molecules themselves. This is typically used in crystals, and produces two peaks in the spectrum, one slightly above the laser frequency, and one below, knows as the Stokes and Anti-Stokes waves respectively. These peaks shift in frequency due to pressure and temperature variation inside the crystal. The difference between Brillouin and Raman scattering, is that Raman scattering is an effect related to individual molecules, while Brillouin backscattering looks at waves among groups of atoms (phonons). Raman backscattering has seen applications in nanotechnology and Material science (Das and Agrawal, 2011).

The equation describing Raman backscattering frequency change ($\Delta\omega_R$) in the case where strain is biaxially isotropic, i.e. $\epsilon_{\text{xx}} = \epsilon_{\text{yy}}$ (Callsen et al., 2011), is:

$$\Delta\omega_R = 2\ a\ \epsilon_{\text{xx}} + b\ \epsilon_{\text{zz}} \tag{2.4}$$

Where ϵ is strain, and a and b are coefficients which depend on the elastic stiffness, and are typically experimentally derived for various compounds which could be used in a doped optical-fibre, crystal or similar set-up.

While a strain relationship exists, Raman scattering is not commonly utilised in fibre strain sensing tools. The reason for this is that the signal is very low amplitude, as well as very broad gain function (about 10 THz). To circumvent the low amplitude issue, implementations of Raman scattering in fibres often utilise Stimulated Raman Scattering (SRS) (Boyd, 2008, Chapter 8), however this transfers power from the source into Raman spectra, which limits the range of a sensor to only a few hundred meters.

Raman scatterings broad gain function could be made more narrow by using doped fibres. As seen in Galeener et al. (1987), silicon behaves rather poorly, in that its Raman gain function is very broad and not very strong compared to other materials. Further research is required to examine the strain sensitivity of each of these materials.

2.2.3 Review of Rayleigh Scattering

Rayleigh scattering is the direct scattering of laser pump photons from the inhomogeneities that constitute a optical fibre, occurring from electron-photon interaction. In optical fibres, Rayleigh scattering results in a fraction of the laser pump power to be lost for every unit length. In telecommunication applications this is considered detrimental to the operation of the cable, since power is being lost. Recently there have been applications of this phenomenon where this scattering can be used to measure the cable's temperature and strain, at any point in the cable.

2.2.3.1 Polarisation Optical Time Domain Reflectometry Systems

The Polarisation Optical Time Domain Reflectometry (Polarisation-OTDR) concept was first published by Rogers (1981), highlighting how the elasto-optic effect of a fibre optical cable can be used to detect changes in its surrounding, which create changes in the cable's birefringence. He highlighted that optical fibre would be highly sensitive to strain changes, but it would also be highly sensitive to surrounding electric, magnetic and temperature variation.

In theory a Down-Hole pressure monitor could be designed using Polarisation-OTDR, where surrounding magnetic fields causing birefringence in the optic cable would be suppressed. For in-situ stress monitoring, magnetic fields are static over time, this should not impede data acquisition.

Based on this concept, a vibration sensor could be constructed (Zhang and Bao, 2008). It was shown that multiple frequency events could be detected in a fibre section, across a very broad bandwidth (1 to 5000 Hz), but is limited by the fact that the detection had to integrate 1.5 seconds (100 pulses) of data. This was achieved by studying the amplitude changes of backscattering over a period of time. In an acoustic detector, the pressure sensitive section of a cable longer than an infinitesimal point, and use the length of the cable for averaging, giving many points to average across such that there is no need to average as many pulses over time.

In more recent work by Han et al. (2007), Polarisation-OTDR sensors are shown to have greatly improved signal to noise ratio (SNR) and operational range by generating so called grating-assisted Polarisation-OTDR. This is achieved by fabricating uniformly distributed weak Fibre Bragg Gratings (FBGs), with FBG intervals on the order of the laser pulse width. This is done in order to improve the strength of reflections from the fibre and the amplitude of backscattered signal. Han

et al. (2007) shows that this gives nearly 10 times more accurate readings of fibre bend radius around a mandrel. In a distributed system the FBGs would need to be inscribed only in areas where the sensor is located, due amplitude over length losses.

Concerning potential development in Polarisation-OTDR for a seismic sensor (or hydrophone), the long detection time cripples the ability of a sensor to detect pressure changes on the order of seismic sampling rates (2 to 4 ms).

Lu et al. (2010) state, in their paper on Phase-OTDR (Phase Optical Time Domain Reflectometry), that detecting the size of a disturbance with Polarisation-OTDR is prevented by the polarisation evolution along the fibre. Further more, Qin et al. (2012) point out that after the detection of a vibration, backscattered signals beyond the point of first detection are contaminated by previous perturbations, meaning distributed seismic sensing is not possible using Polarisation-OTDR. As such, other Rayleigh based systems have polarisation control methods to eliminate noise originating from polarisation changes in the cable.

2.2.3.2 Phase Optical Time Domain Reflectometry (Phase-OTDR) Systems

Phase Optical Time Domain Reflectometry (Phase-OTDR) is achieved by detecting the phase of the Rayleigh backscatter at any point in the fibre cable. Although not a frequency shifting process, it is discussed here because it has good potential as a distributed compact strain sensing sensor. Signal from strained or vibrated points in the fibre is frequency shifted using an Acousto-Optic Modulator (AOM), and mixed with the Local Oscillator, or pump, in a heterodyne, which preserves phase information, at an intermediate frequency defined by the difference between the pump and the reflected signal shifted by the AOM. Lu et al. (2010) published a distributed Phase-OTDR sensing system capable of sensing frequencies between 5 Hz and 1kHz, with sampling intervals as short as 10 microseconds, depending on desired SNR. This is not far from the sampling rates required by seismic acquisition. In other publications (Hui et al., 2013), the AOM is replaced by a Mach-Zehnder Electro-Optic Modulator (EOM) to provide better spacial resolution, however this requires further processing to correct for its drifts in frequency.

SNR ratio is limited by both shot noise as well as thermal fluctuations in the fibre. Wavelet denoising methods implemented by Qin et al. (2012) illustrate that SNR can be improved by having a wavelet model, rather than using moving average over several detections, providing potential for extremely fast sampling rates of signals, and very broad frequency detection potential. In their paper they presented detection of 20 Hz and 8 kHz signal. Although frequencies that high are not required by seismic sensors, this implies that such sensors can have much wider applicability.

Implementation of Phase-OTDR as a seismic-sensor seems very possible in theory. Decent spacial resolution, long maximum length, and vibration frequency bandwidth covering seismic frequencies and beyond are all ideal qualities for a seismic sensor, provided required sampling rates can be reached. Building a sensor can be achieved by spooling sections of fibre around a mandrel in a localised point, and averaging the frequency content of vibrations of the cable along the length of the spooled area. Thus SNR and sampling rate issues can be mitigated using more cable in a detector.

As this method of strain detection is not in-line with this thesis, Phase-OTDR Systems is not discussed further, however it should be noted as a point of further research in the future.

2.2.3.3 Optical Frequency Domain Reflectometry (OFDR) Rayleigh scattering Systems

When modelling Rayleigh scattering in a strain measurement context, it is useful to consider this scattering as a set of random Bragg gratings, all along the cable, giving weak backscatter at a range of frequencies in an approach first considered by Froggatt and Moore (1998). Using a Tunable Laser Source (TLS), they showed that for any point in the cable, the shifted state of the frequency spectrum defines its stress state. Applying strain to the cable would result in the shifting of the spectrum, which they illustrated by cross-correlating the spectrum of a point in the cable in the unstressed state to its stressed state. One of the most attractive aspects of this way of detecting strain, is that a detector may be defined from any collection of points along the fibre, where averaging the strains along a section of fibre improves the SNR, at the cost of having to average a longer section of cable.

Froggatt and Moore (1998) highlighted the drawbacks of such a system, which illustrate that this would be unsuitable for application as a seismic detector. These drawbacks were: detection was limited to less than 100m, due to laser dispersion making analysis impossible; strain sensitivity is no better than Fibre Bragg Gratings; the system had a very poor signal to noise ratio (SNR); and TLS takes a whole second to complete its sweep, meaning sample rates of 2ms are outright impossible with simple TLS based devices. The advent of distributed Bragg reflector (DBR) lasers, meant that sweeping though a range of up to about 80 nm can be done on the order of 100's of nanoseconds (Piprek, 2005, Chapter 6), though it a stepwise manner.

Ding et al. (2012) illustrated a vibration sensor reaching lengths of 12 km, which is practical for seismic purposes, although his results suffered from very poor signal to noise ratio (as low as approximately 1.5) when measuring the frequency of vibrations at more than one location in the cable. Their work considered only semi-permanent vibration sources, where having a long time to complete a TLS sweep was available.

Improvements in strain sensitivity were illustrated by Wang et al. (2012b) where they used a tapered length of cable to show that it's temperature and strain sensitivity can be dramatically improved, for a single mode fibre. They show an impressive strain sensitivity of 17.17 nm/mϵ, whereas Froggatt and Moore (1998) showed $1.5 - 2.5$ nm/mϵ for what must be assumed to be a similar non-tapered fibre. Wang et al. (2012a) discusses the theory, where the effect of the taper is the introduction of higher order modes in the fibre in the area in or around the taper, depending on how it is tapered. Refractive index changes due to strain can then be measured as the difference in effective refractive indices of a pair of modes, using mode-coupling theory crudely analogous to Fibre-Bragg-Gratings or Long-Period-Gratings. Previous work in this field (Fielding et al., 1999) experimentally shows how creating the taper in the fibre can force the core mode to propagate in the cladding, where it would no longer act as a single mode fibre, allowing for power to transfer to other modes, which would then create interference patterns. In this scenario tapering would create a frequency profile that has a consistent peak-trough pattern that is much easier to cross-correlate and would hence improve SNR. Rayleigh backscattering from the tapered sections can show the wavelength shifts at every 13 μm section in the taper. As such there is no need a very long taper section to be able to find the strain value in the taper with very good SNR and a sensitivity that is comparable to sensitivities expected from near turning-point Long-Period-gratings.

Further work on tapered fibres implies that for bent tapered sections sensitivity to external

effects can increase drastically (Sun et al., 2013), an effect similar to the turning point of Long-period-gratings. The paper lacks proper derivation of sensitivity relations, and further research would be required to understand how to fully utilise this property. In the future, incorporating DBR lasers to enable fast tuning, Rayleigh scattering systems with improved sensitivity from tapering could make for good sensors.

2.2.4 Review of White light based Fiber-Optic Extrinsic Fabry-Perot Interferometer

Fabry-Perot cavities are a popular choice for fibre optic interferometric sensor. Extrinsic Fabry-Perot cavities first proposed by (Murphy et al., 1991), are simply Fabry-Perot cavities that are created by creating a small, typically air-filled, space between two sections of fibre. This creates two back reflected pulses, separated by a small difference in phase. In work done by Xiao et al. (2003) the interference pattern, in the frequency domain of light across a broad spectrum, was studied and the first designs for a strain and temperature sensor were established. Since cavities are typically very small, allowing for overall very small sensors, phase detection methods are typically noisy since the phase difference is not shifting significantly with strain, but observing the interference pattern would prove the be hugely advantageous for precision and sensitivity.

Later work done by Shen and Wang (2005) started to tackle the issues of detecting the frequency difference accurately and quickly. Utilising a secondary intrinsic Fabry-Perot cavity, which is significantly more temperature sensitive, meant that absolute changes in the temperature (or strain) of the fibre could be measured by looking at the difference in the frequency of these to adjacent cavities.

Yu and Zhou (2011) provides a good summary of the progress in these cavities since, and proposes a pressure sensor for acoustic wave detection. Spectral detection of shifts in the interference spectrum have been improved by cross-correlation and demodulation algorithms that provide extremely precise cavity length resolution.

Diaphragm extrinsic Fabry-Perot cavities are already utilised as acoustic wave sensors. Sensitivities as high as 1 nm/Pa are reported (Wang et al., 2013), but this falls off rapidly and the gas in the cavity becomes more incompressible with higher pressure. Sensors can be designed such that they operate very well at very specific depths, such as just $10 - 13$ m underwater, claiming a sensitivity of 6.9 nm/Pa while they fall off to 0.11 nm/Pa at depths of 90 m. These are extremely good figures, but these sensors have a couple of crippling downsides. Firstly they are also very temperature sensitive, facing shifts of 333 nm/C$^\circ$ at room temperature. Secondly, sharp changes of the sensitivity with external pressure means that sensors need to be purpose designed, as hydrophones would vary greatly in sensitivity as they float up and down a only few meters.

Nevertheless, extrinsic Fabry-Perot Interferometers should be considered in future discussions of optical geophone/hydrophone development.

2.2.5 Review of Long Period Fibre Grating

2.2.5.1 Description of core and cladding modes

Fibre Bragg Gratings (FBG) in optic cables are used in seismic sensors to create narrow absorption lines which are unique to each detector and used for frequency division multiplexing of large sets

of detectors. When the grating is spaced at short periods, such as in FBG, the absorption line does not shift much with respect to the strain on the cable, and is very narrow (Yu, 2002, Chapter 4). Conversely in the case of Long Period Fibre Gratings (LPFGs), strain sensitivity is shown to be considerably better (Shu et al., 2002) than even Tapered Rayleigh Scattering, however the absorption line becomes much broader.

Long-period-gratings are typically produced in much the same way as Fibre-Bragg-Gratings, the only difference being that the periodicity of the grating is much longer. The effect of this is that core modes couple with co-propagating cladding modes to produce strong transmission losses at specific wavelengths. Long-period-gratings have well understood properties and sensitivity relations (Erdogan, 1997a; Shu et al., 2002).

Shu et al. (2002) identifies conditions where sensitivity of the sensors increases greatly. The following two chapters discuss that with careful design, any optical fibre with any laser can exhibit very high strain sensitivity. The other advantage of these detectors is that they are very small, typically only about 4 cm of fibre-optic cable is required to create a sensor.

The review of the LPFG follows the work of Erdogan (1997a), in the specific case of un-tilted gratings. The diagram below defines what simple step-index fibre-optic cable looks like, adapted from Erdogan (1997a).

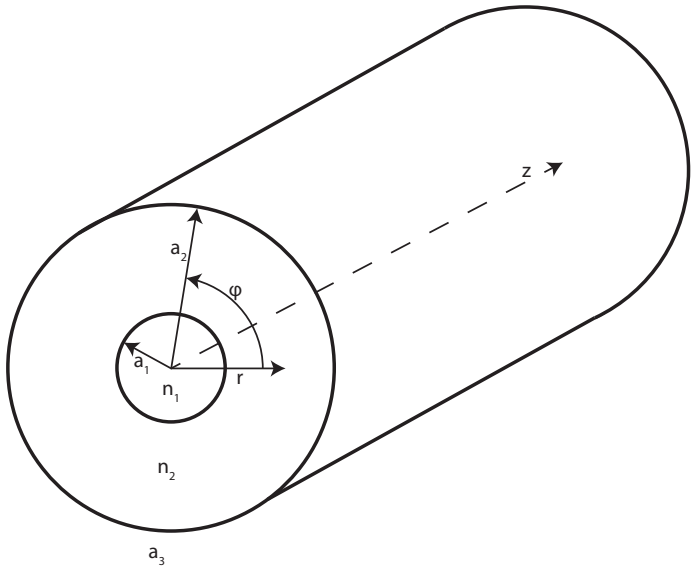

Figure 2.1: Cross sectional diagram of geometric description of a single mode step index optical fibre

In Figure 2.1, n_1,n_2,n_3 are the refractive indices of the core, cladding and external region respectively; and a_1 is the radius of the core, and a_2 is the radius of the cladding.

Light propagating through the core is denoted to be of mode n_{effco}, meaning the effective refractive index of the mode corresponding to the propagation speed through the fibre. These modes have effective refractive indices $n_1 > n_{\text{effco}} > n_2$, since the light bounces off the core-cladding boundary and takes longer to propagate through the fibre than a ray that would pass through a straight fibre section directly. For multi-mode fibres with a large core radius, there can be more than one mode within the core, which would create interference fringes at certain frequencies due

to the other modes.

LPFGs force some light energy into cladding modes, which operate similarly but propagate across the entire radius of the fibre (including the cladding) and have effective refractive indices denoted by n_{effcl}, which have effective refractive indices $n_2 > n_{\text{effcl}} > n_3$.

2.2.5.2 Characteristics of a Long Period Fibre Grating

By evaluating the effective refractive indices of the core and cladding modes, the core-cladding coupling coefficient (κ) for each of the cladding modes can be calculated. This enables the generation of a predicted absorption spectrum for the grating. One of the better ways to produce gratings is with refractive index changes created by exposure to intense UV light, this is what was used by Erdogan (1997a). Gratings can also be produced by periodic changes in the radius of the fibre, and are discussed in Appendix A.

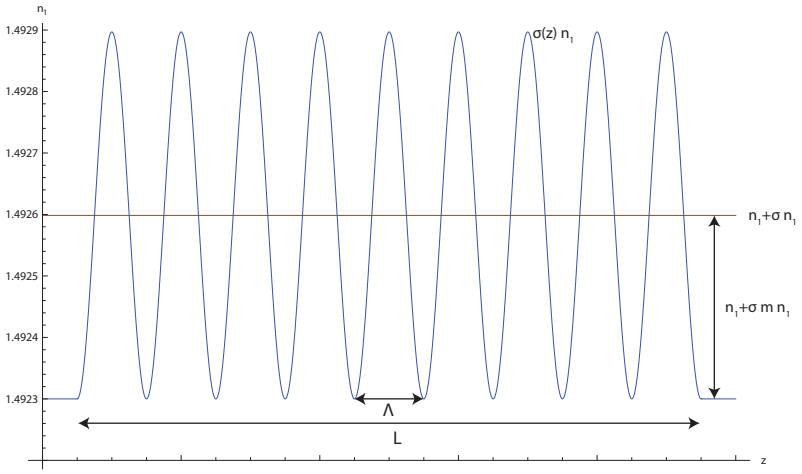

Figure 2.2: Fibre Core refractive index change model for inscribed gratings

In Figure 2.2, σ is the refractive index contrast, m is the fringe modulation, Λ is the grating period, and L is the grating width, in the case of uniformly varying gratings (i.e. σ is a constant). In the Figure 2.2, $\sigma(z)$ is defined as:

$$\sigma(z) = \sigma\left(1 + m\left(Cos\left[\frac{2\pi}{\Lambda}z\right]\right)\right) \tag{2.5}$$

Applying this modulated refractive index model, it is possible to obtain a real value for κ, the mode coupling coefficient. In a paper by Erdogan (1997b), where spectral properties of LPFGs are discussed, the definition of the transmission dip wavelength, λ_D, is:

$$\lambda_D = (n_{\text{effco}} - n_{\text{effcl}})\ \Lambda \tag{2.6}$$

with an ideal grating length of (derived later from Eq. 4.1):

$$L = \frac{\pi}{2\kappa} \tag{2.7}$$

From Eq. 2.6 it is important to realise that at a certain operating laser wavelength, grating period can be chosen in order to select from a set of linearly polarised core-cladding coupled modes.

This is important to keep in mind because a LPFG's strain sensitivity varies with grating period, so if designed with careful consideration to the desired wavelength and mode, a very high sensitivity can be achieved.

2.2.5.3 Strain sensitivity of a Long Period Fibre Grating

Shu et al. (2002) provides a description for LPFG sensitivity to temperature, strain, and external refractive index. The change in absorption peak wavelength per unit strain is defined as:

$$\frac{d\lambda}{d\epsilon} = \gamma\lambda_D \left(1 + \Gamma_{\text{strain}}\right) \tag{2.8}$$

Where:

$$\Gamma_{\text{strain}} = \frac{\eta_{\text{co}} n_{\text{effco}} - \eta_{\text{cl}} n_{\text{effcl}}}{n_{\text{effco}} - n_{\text{effcl}}} \tag{2.9}$$

$$\gamma = \frac{1}{1 - \Lambda \frac{d\Delta \text{n}_{\text{eff}}}{d\lambda}} \tag{2.10}$$

With η_{co} and η_{cl} being functions of the elasto-optic coefficients for the core and cladding materials respectively, and $\Delta \text{n}_{\text{eff}} = n_{\text{effco}} - n_{\text{effcl}}$. γ is the most important variable when considering the LPFG sensitivity as it represents the waveguide dispersion. Waveguide dispersion is the chromatic dispersion arising from waveguide effects; in other words it describes the frequency dependence of the LPFG due to its design. Chapters 3 and 4 is devoted to the discussion of these equations, and the of the non-trivial solution of γ approaching infinity, i.e. finding a mode such that:

$$\frac{1}{\Lambda} = \frac{d\Delta \text{n}_{\text{eff}}}{d\lambda} \tag{2.11}$$

This is called a turning point, and solving this makes it possible to design strain sensors of very high sensitivity. This particular solution is discussed in detail throughout Chapters 3 and 4.

2.3 Discussion of Benefits and Limitations

2.3.1 Brillouin/Raman Scattering

Normally, Raman (and Brillouin) scattering are used in structural strain and temperature sensors (Yu, 2002, Chapter 5), where fast sampling rates are not an issue. Implementing a Raman based distributed sensor to with improved noise characteristics, such that long time averaging is not needed requires greater pump power since typically only 10^{-6} of the pump power is scattered into the Stokes wave. However with increasing pump power there is a point when Stimulated Raman Scattering (SRS) is achieved, where most of the energy is transferred into the Stokes wave (Boyd, 2008). This means that over the length of a cable, the majority of the backscattered signal will be Raman induced. This is also undesirable since the pump power will decrease greatly over a distance. One way to mitigate this issue and plausibly create a sensor is to use doped optical fibres in sections where detection is desired, and choose a power such that SRS is achieved only in those areas.

With respect to strain sensing, Brillouin scattering is very similar to Raman scattering, however it is about 10^3 less sensitive to strain in silicon fibres, but its about 10^3 times stronger and spectrally narrower. In a paper by Zhu et al. (2010), a very good Brillouin scattering based sensor is discussed, using heterodyne detection. The pump source is initially encoded and frequency shifted, allowing heterodyne detection to occur at approximating real-time rates and at great distances with very good spatial resolution, without needing a very strong laser (only 2.1 mW). Detectors like this were the initial goal of this thesis, however other mechanisms (namely the LPFG) promise to be more sensitive as well as stronger in amplitude contrast than either Raman or Brillouin scattering processes. The concept of the heterodyne technique employed by Zhu et al. (2010) could be applied to LPFGs.

2.3.2 Rayleigh Scattering

Rayleigh backscatter mechanisms reviewed in Section 2.2.3, seem to have potential in active distributed sensing. The main challenge to overcome is that Rayleigh signal tends to be of a low amplitude, and hence suffers from poor signal to noise ratio (SNR). Phase-OTDR (Phase Optical Time Domain Reflectometry) seems to be the system most promising for seismic acquisition, since it can operate at a fast sample rate. OFDR (Optical Frequency Domain Reflectometry) systems provide much better SNRs at the cost of detection and processing time since it relies on the slow cross-correlation of a frequency domain spectrum to one of a previous time. This means that in remote monitoring scenarios, such as Down-Hole over long periods, it is an effective method of tracking changes in the strain of any arbitrarily defined piece of the cable, where strains develop quasi-statically over time.

Using a DBR laser to enable fast tuning, a Rayleigh scattering based system employing at Tapered section is decent topic for future experimental research into making the sort of acoustic sensors this thesis is trying to cover.

2.3.3 Long Period Fibre Grating

Frequency change at low pressure can be observed with a heterodyne arrangement, but is inherently not ideal, and Chapter 6 is devoted to this discussion. The problem lies in the fact that for seismic acquisition at sampling rate of 2 ms (500 Hz) is typical. LPFGs are usable as a detectors at such sampling rates in heterodyne arrangements, but run into problems when resolving broad spectral features at a fast speed. Time division multiplexing is the only obvious multiplexing method available, but the heterodyne would need to have enough time to resolve hundreds of detectors if the LPFG was implemented as a hydrophone. Using the simple relation of $\Delta\nu = \frac{1}{2\tau}$, where $\Delta\nu$ is the bandwidth of the heterodyne intermediate bandpass filter and τ is the data collection time (Bingham et al., 1998), there is less time to collect the light when detecting spectral changes across a broader bandwidth. Signal power of LPFGs is very high, which will help mitigate SNR issues that arise from having less time to interrogate the spectrum.

This thesis does not discuss multiplexing methods at length, and is mostly a discussion on the implementation of functioning ideas. So, the main goal is to demonstrate adequate sensitivity of a single detector. However it is important to be mindful that regarding multiplexing LPFGs that wave or frequency division multiplexing is not available since a heterodyne looks at frequency changes.

Resolving small polarisation differences for potentially hundreds of detectors will be impossible for polarisation multiplexing. Time division multiplexing alone cannot be applied to large arrays due to the large collection time required for each detector. Phase division multiplexing is the only other possible multiplexing option. Otherwise large arrays would require a system with many detectors is that work completely independently, and be detected by independent heterodyne arrangements, which is very costly, and will require an individual optical fibre for every channel, which is very cumbersome.

2.4 Sensitivity Summary / Conclusion

Table 2.1: Summary of sensitivities of various OFDR methods

Sensing Mechanism	Sensitivity (nm/mϵ)	Reference
Brillouin backscattering	6.35×10^{-4}	Mizuno et al. (2012)
FBG shift as WDM in Fabry-Perot cavity	1.1	Chen et al. (2009)
Rayleigh backscattering	2.0	Froggatt and Moore (1998)
Rayleigh backscattering, tapered	17.17	Wang et al. (2012b)
Rayleigh backscattering, bent tapered	N/A*	Sun et al. (2013)
LPFG	2.2	James and Tatam (2003)
LPFG, asymmetric grating	7.6	Xiao et al. (2006)
LPFG, near turning point (high γ)	30.31	Shu et al. (2002)

A quick look at the summary of sensitivities that have been discussed so far in this chapter illustrates the main focal point of the research in the chapters to follow. Long Period Fibre Gratings exhibit the most promise as a potential mechanism for hydrophone or depth sensors.

From the point of view of developing a depth pressure sensor, where high sensitivity is of lesser concern, many of these methods are appropriate, as long as they can exhibit low, or ideally near zero, temperature sensitivity.

The strain sensitivity of bent tapered Rayleigh backscattering is yet to be investigated. It functions on a theory not too dissimilar to the coupled-mode theory that defines LPFGs. Since tapered designs already exhibit a high strain sensitivity, and the sensitivity to external refractive index is much higher in bent tapers as illustrated by Sun et al. (2013), it is expected that bent tapered fibres will exhibit excellent strain sensitivity.

The white light extrinsic Fabry-Perot hydrophones actually exhibit pressure sensitivities that are dramatically better than what is expected from simple fibre sensors. The quoted sensitivity of 6.9 nm/Pa by Wang et al. (2013) can be compare to figures derived in Chapter 5 discussing pressure sensitivity of a LPFG wound around a compliant mandrel, where a sensitivity of 0.1 pm/Pa was estimated. However, such a seemingly low sensitivity is sufficient as a heterodyne can easily resolve such shifts in the frequency spectrum. Also, the Fabry-Perot sensor is highly non-linear in its sensitivity, while the LPFG is believed to be somewhat linear is its strain response as evidenced by Shu et al. (2002); Wang et al. (2006).

For these reasons the main method investigated through the remainder of the thesis is the Long Period Fibre Grating, with a goal of designing it such that it operates near a turning point (gratings with high γ, a key variable in defining the sensitivity of gratings).

Chapter 3

Long Period Fibre Grating Theory

3.1 Description of core and cladding modes and Grating Characteristics

Fibre Bragg Gratings (FBGs) in optic cables are used in typical hydrophones to create narrow absorption lines which are unique to each sensor and used for frequency division multiplexing (Grattan and Sun, 2000) of large sets of sensors. When the grating on a very short period, such as in FBGs, the absorption line does not shift much with respect to the strain on the cable, and is very narrow. However in the case of Long Period Fibre Gratings (LPFGs), strain sensitivity is shown to be considerably better (James and Tatam, 2003) even for a LPFG that does not aim to be highly sensitive.

Long Period Gratings can be produced in much the same way as Fibre-Bragg-gratings, the only difference being that the periodicity of the grating is much longer. The effect of this is that core modes couple with co-propagating cladding modes to produce strong losses at specific wavelengths (Erdogan, 1997b), whereas a FBG would create coupling between forward and backward propagating core modes. Long Period Gratings have well understood properties and sensitivity relations (Erdogan, 1997a; Shu et al., 2002), and this chapter looks to cover the mathematical tools needed to solve for the sensitivity of an arbitrary step-index fibre, with any chosen grating period. Other than step-index fibres, Photonic Crystal Fibres (PCF) have been modelled using finite element analysis (Petrovic, 2008) and show promise as temperature insensitive LPFGs (Dobb et al., 2004). These fibres offer excellent control over the modes propagating in the fibre but they are typically made from silicon, whereas this research intends to utilise plastic fibres to achieve a tighter bend radius.

Shu et al. (2002) identifies conditions where sensitivity of the sensors increases greatly, referred to as turning points. This discussion shows that with careful design, every mode can exhibit great strain sensitivity. The cladding modes created in the fibre by the gratings are actually come in pairs, one which couples strongly and the other weakly. The choice between the strong and weakly coupling modes corresponds to a choice between a LPFG with of short length and broad transmission dip, or longer length and narrow transmission dip. Regardless, even long LPFGs are very short, and typically no more than 4 to 8 cm of fibre-optic cable is required to create a sensor.

The review of the LPFG will follow the work of Erdogan (1997a), in the specific case of un-tilted

gratings. Figure 2.1 illustrates the variables that define a step index optical fibre profile, where n_1,n_2,n_3 are the refractive indices of the core, cladding and external region respectively; and a_1 is the radius of the core, and a_2 is the radius of the cladding. Keep in mind that Erdogan (1997a) only considered the case where there period grating refractive index contrast is localised to only the core of the fibre. While this is possible with doped fibres, other methods, especially ones with diameter modulation discussed in Appendix A, its is by no means the most common way to inscribe these gratings.

Firstly, the dispersion relation of the core mode, n_{effco}, of a fibre is defined:

$$V\sqrt{1-b}\frac{J_1\left(V\sqrt{1-b}\right)}{J_0\left(V\sqrt{1-b}\right)} = V\sqrt{b}\frac{K_1\left(V\sqrt{b}\right)}{K_0\left(V\sqrt{b}\right)} \tag{3.1}$$

where, J_n is a Bessel function of the first kind, and K_n is a modified Bessel function of the second kind, and;

$$V = \left(\frac{2\pi}{\lambda}\right) a_1 \sqrt{{n_1}^2 - {n_2}^2} \tag{3.2}$$

$$b = \frac{n_{\text{effco}}^2 - {n_2}^2}{{n_1}^2 - {n_2}^2} \tag{3.3}$$

Hence allowing us to find n_{effco}, which is the effective refractive index of the core mode(s) at a source, or pump, wavelength λ.

Next, the definition for the dispersion relation for the cladding modes, n_{effcl}, which allows for the numerical solution for every cladding mode is:

$$\zeta_0 = \zeta_0' \tag{3.4}$$

where,

$$\zeta_0 = \frac{1}{\sigma_2}\frac{u_2\left(J\ K + \frac{\sigma_1\sigma_2 u_{21}u_{32}}{{n_2}^2 a_1 a_2}\right) p_l\left(a_2\right) - K\ q_l\left(a_2\right) + J\ r_l\left(a_2\right) - \frac{s_l(a_2)}{u_2}}{-u_2\left(\frac{u_{32}\ J}{{n_2}^2 a_2} - \frac{u_{21}\ K}{{n_1}^2 a_1}\right) p_l\left(a_2\right) + \frac{u_{32} q_l(a_2)}{{n_1}^2 a_2} + \frac{u_{21} r_l(a_2)}{{n_1}^2 a_1}} \tag{3.5}$$

$$\zeta_0' = \sigma_1 \frac{u_2\left(\frac{u_{32}\ J}{a_2} - \frac{\left({n_3}^2 u_{21}\right)\ K}{{n_2}^2 a_1}\right) p_l\left(a_2\right) + \frac{u_{32} q_l(a_2)}{a_2} + \frac{u_{21} r_l(a_2)}{a_1}}{u_2\left(\frac{{n_3}^2\ J\ K}{{n_2}^2} + \frac{\sigma_1\sigma_2 u_{21}u_{32}}{{n_1}^2 a_1 a_2}\right) p_l\left(a_2\right) - \frac{{n_3}^2\ K\ q_l(a_2)}{{n_1}^2} + J\ r_l\left(a_2\right) - \frac{{n_2}^2 s_l(a_2)}{{n_1}^2 u_2}} \tag{3.6}$$

where,

$${u_1}^2 \equiv \left(\frac{2\pi}{\lambda}\right)^2 \left({n_1}^2 - {n_{\text{effcl}}}^2\right) \tag{3.7}$$

$${u_2}^2 \equiv \left(\frac{2\pi}{\lambda}\right)^2 \left({n_2}^2 - {n_{\text{effcl}}}^2\right) \tag{3.8}$$

$${w_3}^2 \equiv \left(\frac{2\pi}{\lambda}\right)^2 \left({n_{\text{effcl}}}^2 - {n_3}^2\right) \tag{3.9}$$

$$\sigma_1 \equiv \frac{\mathbb{i} l n_{\text{effcl}}}{Z_0} \tag{3.10}$$

$$\sigma_2 \equiv \mathbb{i} l n_{\text{effcl}} Z_0 \tag{3.11}$$

$$u_{21} \equiv \frac{1}{{u_2}^2} - \frac{1}{{u_1}^2} \tag{3.12}$$

$$u_{32} \equiv \frac{1}{{w_3}^2} + \frac{1}{{u_2}^2} \tag{3.13}$$

$$J \equiv \frac{J_l'(u_1 a_1)}{u_1 J_l(u_1 a_1)} \tag{3.14}$$

$$K \equiv \frac{K_l'(w_3 a_2)}{w_3 K_l(w_3 a_2)} \tag{3.15}$$

$$p_l(r) \equiv J_l(u_2 r) N_l(u_2 a_1) - J_l(u_2 a_1) N_l(u_2 r) \tag{3.16}$$

$$q_l(r) \equiv J_l(u_2 r) N_l'(u_2 a_1) - J_l'(u_2 a_1) N_l(u_2 r) \tag{3.17}$$

$$r_l(r) \equiv J_l'(u_2 r) N_l(u_2 a_1) - J_l(u_2 a_1) N_l'(u_2 r) \tag{3.18}$$

$$s_l(r) \equiv J_l'(u_2 r) N_l'(u_2 a_1) - J_l'(u_2 a_1) N_l'(u_2 r) \tag{3.19}$$

where N_n is a Bessel function of the second kind. In these equations, $l = 1$ since the case of un-tilted gratings is being considered.

Solving Eq. 3.4 for n_{effcl} will yield an infinite set of solutions that are strictly less than n_2. However, only the solutions in the range of (n_2, n_3) are useful. For simplicity, this work looks at the case of $n_3 = 1$. Code for solving this dispersion relation is covered in LPFGcalcLoop.nb, which solves across a range of pump wavelengths at chosen intervals. Solutions from this are later used to find turning points in sensitivity.

Having a set of solutions for effective cladding modes is useful before needing to define a grating period. A normalised coupling coefficient ($\kappa_{normalised}$) can be determined, indicting how well each of the cladding modes will couple to the core mode(s). The stronger the coupling, the less interaction length and grating refractive index contrast are required to create a strong absorption. The normalised coupling coefficient can be generated for each cladding mode, by solving for the pump power distribution in the core (P_1), cladding (P_2), and external regions(P_3), which for the purpose of this work will be air. A normalised total pump power of $1W$ is assumed, i.e.:

$$P_1 + P_2 + P_3 = 1 \tag{3.20}$$

where,

$$\begin{aligned} P_1 = {} & \left(E_{1\nu}^{\text{cl}}\right)^2 \frac{\pi {a_1}^2 {u_1}^2}{4} \\ & \left(\left(\frac{n_{\text{effco}}}{Z_0} - \frac{n_{\text{effco}} Z_0 \zeta_0^2}{{n_1}^2} + \left(1 + \frac{{n_{\text{effco}}}^2}{{n_1}^2}\right) \text{Im}(\zeta_0)\right)\left(J_2(u_1 a_1)^2 - J_1(u_1 a_1) J_3(u_1 a_1)\right) + \right. \\ & \left.\left(\frac{n_{\text{effco}}}{Z_0} - \frac{n_{\text{effco}} Z_0 {\zeta_0}^2}{{n_1}^2} - \left(1 + \frac{{n_{\text{effco}}}^2}{{n_1}^2}\right) \text{Im}(\zeta_0)\right)\left(J_0(u_1 a_1)^2 + J_1(u_1 a_1)^2\right)\right) \end{aligned} \tag{3.21}$$

$$P_2 = \left(E_{1\nu}^{\mathrm{cl}}\right)^2 \frac{\pi^3 {a_1}^2 {u_1}^4 {u_2}^2 J_1\left(u_1 a_1\right)^2}{16} \left(\left(\frac{n_{\mathrm{effcl}}}{Z_0} {F_2}^2 - \frac{n_{\mathrm{effcl}} Z_0}{{n_2}^2} {G_2}^2 \right) \left(Q + \tilde{Q}\right) \right.$$
$$+ \frac{1}{{u_2}^2} \left(\frac{n_{\mathrm{effcl}}}{Z_0} - \frac{n_{\mathrm{effcl}} Z_0 {n_2}^2 {\zeta_0}^2}{{n_1}^4} \right) \left(R + \tilde{R}\right) + \left(1 + \frac{{n_{\mathrm{effcl}}}^2}{{n_2}^2}\right) F_2 \Im\left(G_2\right) \left(Q - \tilde{Q}\right)$$
$$+ \left(1 + \frac{{n_{\mathrm{effcl}}}^2}{{n_2}^2}\right) \frac{{n_2}^2}{{n_1}^2 {u_2}^2} \mathrm{Im}\left(\zeta_0\right) \left(R - \tilde{R}\right)$$
$$\left. - \left(1 + \frac{{n_{\mathrm{effcl}}}^2}{{n_2}^2}\right) \left(\frac{{n_2}^2 \mathrm{Im}\left(\zeta_0\right)}{{n_1}^2 {u_2}^2} F_2 + \frac{1}{{u_2}^2} \mathrm{Im}\left(G_2\right) \right) \left(S - \tilde{S}\right) + \frac{2 n_{\mathrm{effcl}}}{u_2} \left(\frac{Z_0 \zeta_0}{{n_1}^2} G_2 - \frac{1}{Z_0} F_2 \right) \left(S + \tilde{S}\right) \right) \tag{3.22}$$

$$P_3 = \left(E_{1\nu}^{\mathrm{cl}}\right)^2 \frac{\pi^3 a_1^2 {a_2}^2 {u_1}^4 {u_2}^4 J_1\left(u_1 a_1\right)^2}{16 {w_3}^2 K_1\left(w_3 a_2\right)^2} \left(\left(\frac{n_{\mathrm{effcl}} Z_0}{{n_3}^2} {G_3}^2 - \frac{n_{\mathrm{effcl}}}{Z_0} {F_3}^2 \right.\right.$$
$$\left. - \left(1 + \frac{{n_{\mathrm{effcl}}}^2}{{n_3}^2}\right) F_3 \mathrm{Im}\left(G_3\right) \right) \left(K_2\left(w_3 a_2\right)^2 - K_1\left(w_3 a_2\right) K_3\left(w_3 a_2\right) \right)$$
$$\left. + \left(\frac{n_{\mathrm{effcl}} Z_0}{{n_3}^2} {G_3}^2 - \frac{n_{\mathrm{effcl}}}{Z_0} {F_3}^2 + \left(1 + \frac{{n_{\mathrm{effcl}}}^2}{{n_3}^2}\right) F_3 \mathrm{Im}\left(G_3\right) \right) \left(K_0\left(w_3 a_2\right)^2 - K_1\left(w_3 a_2\right)^2 \right) \right) \tag{3.23}$$

These equations need to be solved for the parameter $E_{1\nu}^{\mathrm{cl}}$, which is the field normalisation constant for a specific cladding mode number ν. Z_0 is the electromagnetic impedance in vacuum, i.e. approx 377 Ω:

$$Z_0 = \sqrt{\frac{\mu_0}{\epsilon_0}} \tag{3.24}$$

And the rest of the variables are defined as follows:

$$F_2 = J - \frac{\zeta_0 \sigma_2 u_{21}}{a_1 {n_1}^2} \tag{3.25}$$

$$G_2 = \frac{\sigma_1 u_{21}}{a_1} + \zeta_0 J \tag{3.26}$$

$$F_3 = \frac{q_1\left(a_2\right)}{u_2} - F_2 \; p_1\left(a_1\right) \tag{3.27}$$

$$G_3 = -\frac{{n_3}^2}{{n_2}^2} \left(G_2 \; p_1\left(a_2\right) - \frac{\zeta_0 {n_2}^2 q_1\left(a_2\right)}{{n_1}^2 u_2} \right) \tag{3.28}$$

$$Q = \theta_J Y_1\left(a_1 u_2\right)^2 - 2\theta_{\mathrm{JN}} J_1\left(a_1 u_2\right) Y_1\left(a_1 u_2\right) + \theta_N J_1\left(a_1 u_2\right)^2 \tag{3.29}$$

$$\tilde{Q} = \tilde{\theta_J} Y_1\left(a_1 u_2\right)^2 - 2\tilde{\theta_{\mathrm{JN}}} J_1\left(a_1 u_2\right) Y_1\left(a_1 u_2\right) + \tilde{\theta_N} J_1\left(a_1 u_2\right)^2 \tag{3.30}$$

$$R = \frac{1}{4}\theta_J \left(Y_2\left(a_1 u_2\right) - Y_0\left(a_1 u_2\right)\right)^2 - \frac{1}{2}\theta_{\mathrm{JN}} \left(J_2\left(a_1 u_2\right) - J_0\left(a_1 u_2\right)\right) \left(Y_2\left(a_1 u_2\right) - Y_0\left(a_1 u_2\right)\right)$$
$$+ \frac{1}{4}\theta_N \left(J_2\left(a_1 u_2\right) - J_0\left(a_1 u_2\right)\right)^2 \tag{3.31}$$

$$\tilde{R} = \frac{1}{4}\tilde{\theta_J} \left(Y_2\left(a_1 u_2\right) - Y_0\left(a_1 u_2\right)\right)^2 - \frac{1}{2}\tilde{\theta_{\mathrm{JN}}} \left(J_2\left(a_1 u_2\right) - J_0\left(a_1 u_2\right)\right) \left(Y_2\left(a_1 u_2\right) - Y_0\left(a_1 u_2\right)\right)$$
$$+ \frac{1}{4}\tilde{\theta_N} \left(J_2\left(a_1 u_2\right) - J_0\left(a_1 u_2\right)\right)^2 \tag{3.32}$$

$$
\begin{aligned}
S = & \frac{1}{2}\theta_J Y_1\left(a_1 u_2\right)\left(Y_0\left(a_1 u_2\right) - Y_2\left(a_1 u_2\right)\right) \\
& - \frac{1}{2}\theta_{\mathrm{JN}}\left(\left(J_0\left(a_1 u_2\right) - J_2\left(a_1 u_2\right)\right) Y_1\left(a_1 u_2\right) + J_1\left(a_1 u_2\right)\left(Y_0\left(a_1 u_2\right) - Y_2\left(a_1 u_2\right)\right)\right) \\
& + \frac{1}{2}\theta_N J_1\left(a_1 u_2\right)\left(J_0\left(a_1 u_2\right) - J_2\left(a_1 u_2\right)\right)
\end{aligned} \tag{3.33}
$$

$$
\begin{aligned}
\tilde{S} = & \frac{1}{2}\tilde{\theta_J} Y_1\left(a_1 u_2\right)\left(Y_0\left(a_1 u_2\right) - Y_2\left(a_1 u_2\right)\right) \\
& - \frac{1}{2}\tilde{\theta_{\mathrm{JN}}}\left(\left(J_0\left(a_1 u_2\right) - J_2\left(a_1 u_2\right)\right) Y_1\left(a_1 u_2\right) + J_1\left(a_1 u_2\right)\left(Y_0\left(a_1 u_2\right) - Y_2\left(a_1 u_2\right)\right)\right) \\
& + \frac{1}{2}\tilde{\theta_N} J_1\left(a_1 u_2\right)\left(J_0\left(a_1 u_2\right) - J_2\left(a_1 u_2\right)\right)
\end{aligned} \tag{3.34}
$$

where,

$$
\theta_J = {a_2}^2\left(J_2\left(a_2 u_2\right)^2 - J_1\left(a_2 u_2\right) J_3\left(a_2 u_2\right)\right) - {a_1}^2\left(J_2\left(a_1 u_2\right)^2 - J_1\left(a_1 u_2\right) J_3\left(a_1 u_2\right)\right) \tag{3.35}
$$

$$
\theta_N = {a_2}^2\left(Y_2\left(a_2 u_2\right)^2 - Y_1\left(a_2 u_2\right) Y_3\left(a_2 u_2\right)\right) - {a_1}^2\left(Y_2\left(a_1 u_2\right)^2 - Y_1\left(a_1 u_2\right) Y_3\left(a_1 u_2\right)\right) \tag{3.36}
$$

$$
\begin{aligned}
\theta_{\mathrm{JN}} = & {a_2}^2\left(J_2\left(a_2 u_2\right) Y_2\left(a_2 u_2\right) + \frac{1}{2}\left(-J_3\left(a_2 u_2\right) Y_1\left(a_2 u_2\right) - J_1\left(a_2 u_2\right) Y_3\left(a_2 u_2\right)\right)\right) \\
& - {a_1}^2\left(J_2\left(a_1 u_2\right) Y_2\left(a_1 u_2\right) + \frac{1}{2}\left(-J_3\left(a_1 u_2\right) Y_1\left(a_1 u_2\right) - J_1\left(a_1 u_2\right) Y_3\left(a_1 u_2\right)\right)\right)
\end{aligned} \tag{3.37}
$$

$$
\tilde{\theta_J} = {a_2}^2\left(J_1\left(a_2 u_2\right)^2 + J_2\left(a_2 u_2\right)^2\right) - {a_1}^2\left(J_1\left(a_1 u_2\right)^2 + J_2\left(a_1 u_2\right)^2\right) \tag{3.38}
$$

$$
\tilde{\theta_N} = {a_2}^2\left(Y_1\left(a_2 u_2\right)^2 + Y_2\left(a_2 u_2\right)^2\right) - {a_1}^2\left(Y_1\left(a_1 u_2\right)^2 + Y_2\left(a_1 u_2\right)^2\right) \tag{3.39}
$$

$$
\tilde{\theta_{\mathrm{JN}}} = {a_2}^2\left(J_0\left(a_2 u_2\right) Y_0\left(a_2 u_2\right) + J_1\left(a_2 u_2\right) Y_1\left(a_2 u_2\right)\right) - {a_1}^2\left(J_0\left(a_1 u_2\right) Y_0\left(a_1 u_2\right) + J_1\left(a_1 u_2\right) Y_1\left(a_1 u_2\right)\right) \tag{3.40}
$$

$E_{1\nu}^{\mathrm{cl}}$, Eq. 3.20, plays an important part in calculating the coupling coefficient, κ. It is useful to calculate $\kappa_{normalised}$ since the grating profile function ($\sigma(z)$, illustrated in Figure 2.2) can be chosen later to optimise the absorption bandwidth of the chosen mode.

$$
\kappa_{normalised} \equiv \frac{\kappa}{\sigma(z)} \tag{3.41}
$$

$$
\kappa_{normalised} = \frac{1}{2}\ {n_1}^2\ \omega\ \epsilon_0\left(\int_0^{2\pi}\int_0^{a_1} r\left(E_r^{\mathrm{cl}}\left(E_r^{\mathrm{co}}\right)^* + E_\phi^{\mathrm{cl}}\left(E_\phi^{\mathrm{co}}\right)^*\right) dr d\phi\right) \tag{3.42}
$$

where variables in the equation are as defined as follows:

$$
\omega = \frac{2\pi}{\lambda} \tag{3.43}
$$

$$
\Delta = \frac{n_1 - n_2}{n_1} \tag{3.44}
$$

$$
E_r^{\mathrm{co}} = \mathbb{i}\ E_{01}^{\mathrm{co}}\ J_0\left(\frac{\sqrt{1-b}\ r\ V}{a_1}\right) e^{\mathbb{i}\left(\beta_{01}^{\mathrm{co}}\ z - \omega\ t\right) + \mathbb{i}\phi} \tag{3.45}
$$

$$E_{\phi}^{\mathrm{co}} = -E_{01}^{\mathrm{co}}\ J_0\left(\frac{\sqrt{1-b}\ r\ V}{a_1}\right) e^{\mathbb{i}\left(\beta_{01}^{\mathrm{co}}\ z-\omega\ t\right)+\mathbb{i}\phi} \tag{3.46}$$

$$E_r^{\mathrm{cl}} = \frac{1}{2}\ \mathbb{i}\ u_1\ E_{1\nu}^{\mathrm{cl}}\left(-\frac{\zeta_0\sigma_2\left(J_2\left(ru_1\right)-J_0\left(ru_1\right)\right)}{n_1^2}+J_0\left(ru_1\right)+J_2\left(ru_1\right)\right) e^{i\left(\beta_{01}^{\mathrm{co}}\ z-\omega\ t\right)+\mathbb{i}\phi} \tag{3.47}$$

$$E_{\phi}^{\mathrm{cl}} = \frac{1}{2}\ u_1\ E_{1\nu}^{\mathrm{cl}}\left(-\frac{\zeta_0\sigma_2\left(J_0\left(ru_1\right)+J_2\left(ru_1\right)\right)}{n_1^2}-J_0\left(ru_1\right)+J_2\left(ru_1\right)\right) e^{\mathbb{i}\left(\beta_{01}^{\mathrm{co}}\ z-\omega\ t\right)+\mathbb{i}\phi} \tag{3.48}$$

$$E_{01}^{\mathrm{co}} = \left(\frac{Z_0\ b}{\pi\ n_2\sqrt{1+2b\Delta}}\right)^{\frac{1}{2}} \frac{1}{a_1 J_1\left(V\sqrt{1-b}\right)} \tag{3.49}$$

$$\beta_{01}^{\mathrm{co}} = \frac{2\pi n_{\mathrm{effco}}}{\lambda} \tag{3.50}$$

As discussed in Erdogan (1997a), Eq. 3.42 gives results that vary from the following equation by a constant, so it is used to make numerical calculations significantly easier:

$$\begin{aligned}\kappa_{normalised} = \frac{2\pi}{\lambda}\left(\frac{\pi b}{Z_0 n_2\sqrt{1+2b\Delta}}\right)^{\frac{1}{2}} \frac{{n_1}^2 u_1}{u_1^2-\frac{V^2(1-b)}{{a_1}^2}}\left(1\right.\\ \left.+\frac{\sigma_2\zeta_0}{{n_1}^2}\right) E_{1\nu}^{\mathrm{cl}}\left(u_1 J_1\left(u_1 a_1\right)\frac{J_0\left(V\sqrt{1-b}\right)}{J_1\left(V\sqrt{1-b}\right)}-\frac{V\sqrt{1-b}}{a_1}J_0\left(u_1 a_1\right)\right)\end{aligned} \tag{3.51}$$

This is the equation that is used in this work for evaluating the coupling coefficients, and gives correct solutions. Code solving the coupling coefficients for all modes calculated for a range of wavelengths is provided in LPFGcalcLoop.nb.

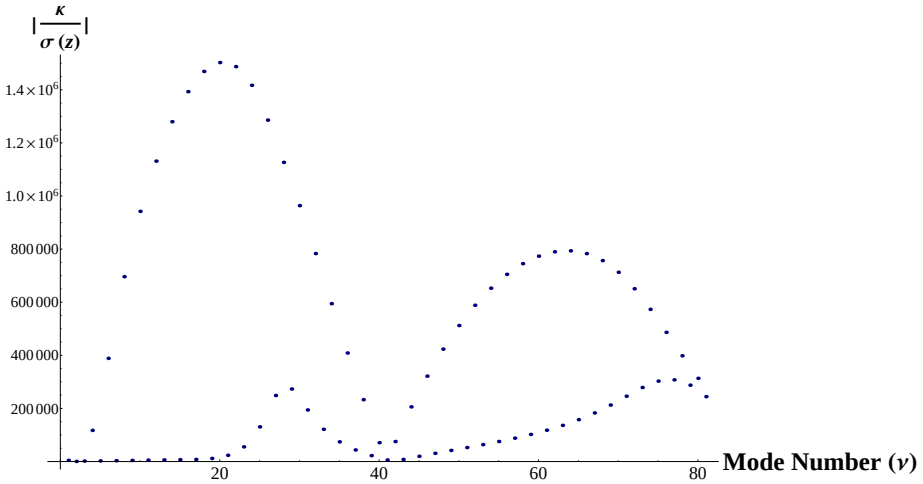

Figure 3.1: Absolute value of the normalised coupling coefficient for the first 81 cladding modes that couple with the fundamental core mode of single-mode PMMA fibre at pump wavelength 600 nm.

Coupling coefficients illustrated in Fig. 3.1 show the LPFG's characteristic coupling differences between odd and even modes. The main effect of higher coupling coefficients is that they create strongly coupling modes create much deeper and broader transmission dips, while weakly coupled modes create smaller and narrower transmission dips. At high mode numbers, especially for silicon fibre, this difference becomes less pronounced.

Having defined the effective refractive indices of the core and cladding modes, and knowing the core-cladding coupling coefficients for all the cladding modes, a predicted absorption spectrum can be generated for an grating with known parameters. One of the better ways to produce gratings is with refractive index changes created by exposure to intense UV light, this is what was used by Erdogan (1997a). Gratings can also be produced by periodic changes in the radius of the fibre through electric-arc discharge methods, and will be discussed in Appendix A.

Applying the modulated grating index profile seen previously in Figure 2.2, a real value for κ can be obtained. In a paper by Erdogan (1997b), where the spectral properties of LPFGs are discussed, the absorption peak wavelength is defined as:

$$\lambda_D = (n_{\text{effco}} - n_{\text{effcl}})\,\Lambda \tag{3.52}$$

and an ideal grating length of (this is derived in the next section):

$$L = \frac{\pi}{2\kappa} \tag{3.53}$$

A uniform grating profile is expressed as:

$$\kappa = \kappa_{normalised}\ \sigma \left[1 + m\ Cos\left(\frac{2\pi}{\Lambda} z\right)\right], \tag{3.54}$$

where z is the length of the grating which is an integer multiple of Λ. Taking into account the grating index profile, κ now depends maximum refractive index change due to the LPFG, σ. Hence the condition of ideal bandwidth, Eq. 3.53, can be expanded as:

$$L = \frac{\pi}{2\kappa_{normalised}\,(1+m)\,\sigma}, \tag{3.55}$$

where m = 1, is the "induced-index fringe modulation".

These are all to tools needed to calculate the absorption spectrum for each mode. In the Chapter 4 these equations are used visualise the absorption spectra for the solutions of high strain sensitivity to illustrate the effects of choosing between coupling strongly or weakly coupled modes.

Figure 3.2 is a good example of the sort of absorption spectrum that can be expected to be generated from a strongly coupling cladding mode. This profile becomes broader if the number of grating periods is lower, and narrower if the number of grating periods is greater. However, this particular spectrum aims at what is considered the ideal bandwidth, so if there were to have more grating periods, the spectrum would being to resemble an envelope of thin absorption lines.

3.2 Strain sensitivity of a Long Period Fibre Grating

Shu et al. (2002) provides a description for LPFG sensitivity to temperature, strain, and external refractive index. The change in absorption peak wavelength per unit strain is defined as:

$$\frac{d\lambda_D}{d\epsilon} = \gamma\lambda_D\,(1 + \Gamma_{\text{strain}}) \tag{3.56}$$

where,

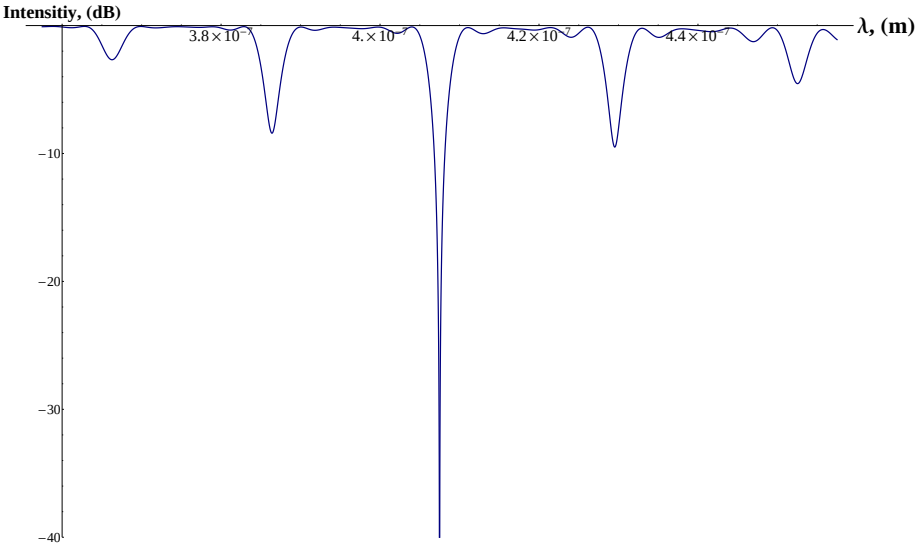

Figure 3.2: The absorption spectrum created by a LPFG with strong coupling

$$\Gamma_{\text{strain}} = \frac{\eta_{\epsilon_{\text{co}}} n_{\text{effco}} - \eta_{\epsilon_{\text{cl}}} n_{\text{effcl}}}{n_{\text{effco}} - n_{\text{effcl}}} \tag{3.57}$$

$$\gamma = \frac{1}{1 - \Lambda \frac{d\Delta \text{n}_{\text{eff}}}{d\lambda}} \tag{3.58}$$

with $\eta_{\epsilon_{\text{co}}}$ and $\eta_{\epsilon_{\text{cl}}}$ being functions of the elasto-optic coefficients for the core and cladding materials respectively, and $\Delta n_{\text{eff}} = n_{\text{effco}} - n_{\text{effcl}}$. $\eta_{\epsilon_{\text{co}}}$ and $\eta_{\epsilon_{\text{cl}}}$ are defined by the following, depending on their refractive index, $n = n_1$ or n_2 respectively:

$$\eta_\epsilon = -\frac{1}{2} n^3 \left(p_{12} - \mu \left(p_{12} + p_{11} \right) \right) \tag{3.59}$$

The coefficients p_{11} and p_{12} are experimentally derived for a range of materials (Adachi, 2005, Chapter 11) and μ is the Poisson Ratio of the fibre. Now, the non-trivial solution of γ approaching infinity will be evaluated, i.e. finding a mode such that:

$$\frac{1}{\Lambda} = \frac{d\Delta \text{n}_{\text{eff}}}{d\lambda} \tag{3.60}$$

at a laser wavelength, λ, coincides with the grating design wavelength, λ_D, such that:

$$\lambda \approx \lambda_D = \Delta n_{\text{eff}} \Lambda \tag{3.61}$$

Implying,

$$\frac{\Delta n_{eff}}{\lambda} \approx \frac{d\Delta n_{\text{eff}}}{d\lambda} \tag{3.62}$$

finally arriving at:

$$\frac{\Delta n_{\text{eff}}}{\lambda} - \frac{d\Delta n_{\text{eff}}}{d\lambda} \to 0 \tag{3.63}$$

This gives a single solution for each mode, at a specific wavelength, giving the some flexibility in designing gratings, as choosing the coupling strength allows the desired grating length and transmission dip width to be chosen to suit the various detector designs. These solutions are referred to as turning points by Shu et al. (2002), and imply that the mode is infinitely sensitive in a positive and negative direction concurrently, which is obviously not physically possible. Instead it is more useful to aim at a solution just off the turning point, though as discussed in Section 7.1, even that is difficult.

Calculating $\frac{d\Delta n_{\text{eff}}}{d\lambda}$ can only be done numerically for any λ, so it is derived by solving Δn_{eff}, for a large set of λ values separated by small changes in λ to make later interpolation more accurate. The solutions determine what pump wavelength, λ, and what grating period, Λ, are needed to be exactly on a turning point.

3.3 Conclusion

Long Period Fibre Grating theory is well established for single mode step-index fibres, and thanks to the contributions from Erdogan (1997a) numerical solutions of the coupling constants of the cladding modes is possible. Shu et al. (2002) goes on to illustrate how there are solution with very high sensitivity, i.e. turning points. Here, a definition for these turning points in Eq. 3.63 is derived, that can be used to find solutions numerically.

LPFGeval.nb in conjunction with LPFGcalcLoop.nb go about finding and interpolating said turning point solutions for every mode across the range of pump wavelengths where the fibre has low attenuation.

The following chapter goes on to discuss how these solutions are useful for the choice plastic fibre (PMMA), but the code can be altered to cope with fibre of any material.

Chapter 4

Long Period Fibre Grating Solution Implementation

4.1 Turning Point Solutions

Using the theory described in the previous chapter, it is possible to solve for the mode coupling coefficient and strain sensitivity of the fibre at any wavelength for every cladding mode. Figure 4.1, is one such solution, plotted for the range of wavelengths where PMMA fibre has lowest attenuation, up to the 63rd mode at every 0.5 nm pump interval. It is necessary to evaluate this numerically at small intervals of wavelength because, as discussed in the previous chapter and appended code, it is only possible to solve for the cladding modes numerically and to improve the results of interpolation, more points are desirable.

Figure 4.1 is the most descriptive representation of the work done on LPFGs in this thesis. It highlights where the solutions for high sensitivity lie for every mode in red and shows what the coupling constants would be. The modes are to calculated for small intervals of pump wavelength ,λ, and the coupling coefficients of every mode form smooth curves. Hence it follows that curves along modes can be interpolated to derive the exact solutions, where $\lambda = \lambda_D$ exactly rather than approximately. This allows the creation a table of solutions for every mode, namely Table 4.1, detailing the coupling constant and exact wavelength at which the solution lies.

Aiming for a solution just off resonance will give the desired high sensitivity, but this carries with it some implications regarding uncertainty which are explored in Chapter 7. Around the turning point solutions choosing a slightly longer or shorter grating period, Λ, will give large positive or negative sensitivities, determined by γ in Eq. 3.58.

4.2 Spectral Characteristics

Modes that have a very strong coupling coefficient evaluate to having very broad absorption but very deep features as the bandwidth, $\frac{\Delta\lambda}{\lambda}$. This bandwidth is a function of the coupling coefficient, κ, as illustrated by Eq. 4.1 (Erdogan, 1997b):

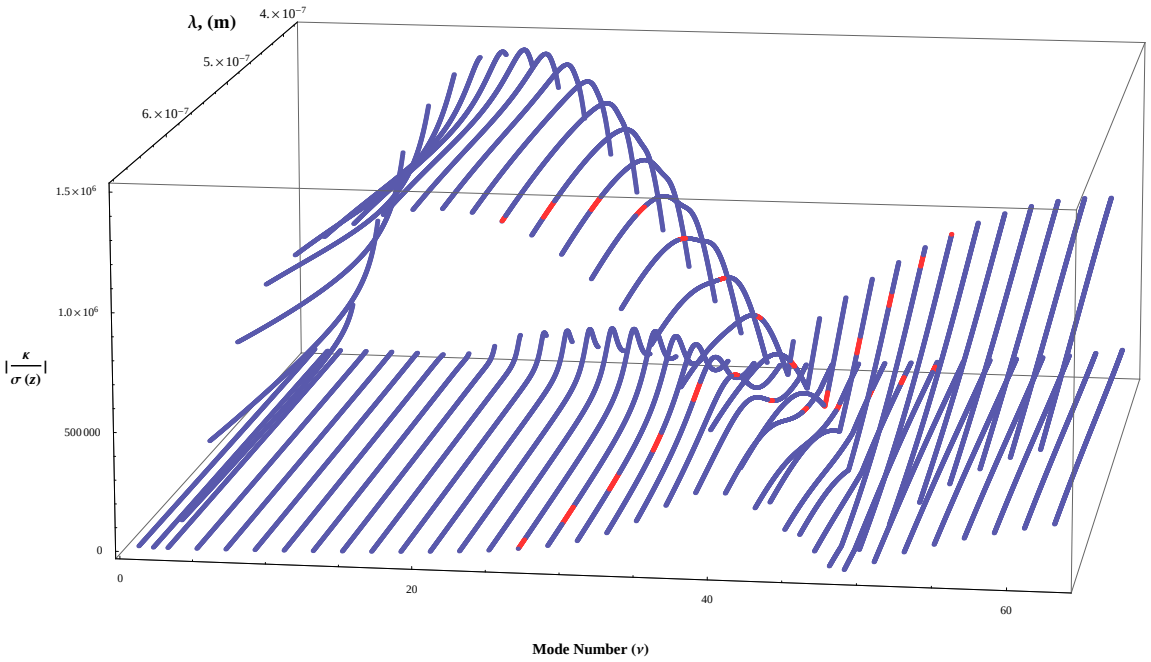

Figure 4.1: Coupling coefficients per cladding modes coupling with the fundamental core mode, given for a range of pump frequencies. Regions in red highlight high sensitivity modes, corresponding to being near turning points

$$\frac{\Delta\lambda}{\lambda} = \frac{2\lambda}{\Delta n_{eff} L}\sqrt{1 - \left(\frac{\kappa L}{\pi}\right)^2} \tag{4.1}$$

The κ in this equation is the non-normalised κ, and is a function of the LPFG inscription strength. Inscriptions strength is measured as the refractive index contrast (σ) in the core of the fibre, and using methods such in Kim et al. (2002) contrasts are typically between 8×10^{-5} and 2×10^{-4}. Consequently, the refractive index contrast required to create a theoretically ideal bandwidth from Eq. 4.1 can be calculated, namely the condition stated in Eq. 3.53, and the relationship to σ was discussed previously in Eq. 3.42.

The distinction between the solutions for each mode is fairly trivial, namely that for strongly coupled modes, with shorter lengths (i.e. less inscribed periods), the transmission dip is much deeper and spread more broadly, as illustrated by Fig. 4.2.

In the code appendices is a notebook which solves the required refractive index contrast needed for any desired length of fibre grating (bandwidthcalc.nb), lists the available solutions between $\sigma = 8 \times 10^{-5}$ and 2×10^{-4} and then plots the absorption spectrum of a chosen solution. For longer desired lengths, modes with lower coupling coefficients are found.

With very weakly coupling modes such as in Fig. 4.3, the lengths needed become quite large, which not only makes the gratings harder to produce, but when calculating the interferences of all the other modes,the spectrum becomes significantly more interesting due to other weakly coupled modes.

Despite this, longer gratings with modestly lower coupling strength produce much sharper overall spectral features than gratings with higher coupling strength. This is the reason why mode 31 was

Table 4.1: Interpolated solutions for every mode across the range of frequencies where PMMA has spectral attenuation

Mode number	Wavelength ($\lambda = \lambda_D$) (m)	Period Grating (Λ) (m)	Coupling coefficient (κ)
28	644.60×10^{-9}	238.57×10^{-6}	1.37421×10^{6}
29	637.73×10^{-9}	235.89×10^{-6}	64849.4
30	606.58×10^{-9}	217.43×10^{-6}	1.30810×10^{6}
31	598.54×10^{-9}	215.96×10^{-6}	95363.7
32	571.17×10^{-9}	199.77×10^{-6}	1.19203×10^{6}
33	564.24×10^{-9}	199.09×10^{-6}	169087
34	538.43×10^{-9}	184.83×10^{-6}	991733
35	535.16×10^{-9}	184.55×10^{-6}	314221
36	509.53×10^{-9}	172.02×10^{-6}	742505
37	509.52×10^{-9}	171.83×10^{-6}	317805
38	484.03×10^{-9}	160.87×10^{-6}	511430
39	486.72×10^{-9}	160.62×10^{-6}	141853
40	461.77×10^{-9}	151.04×10^{-6}	240461
41	465.80×10^{-9}	150.67×10^{-6}	41186.3
42	442.15×10^{-9}	142.27×10^{-6}	13970.8
43	446.05×10^{-9}	141.81×10^{-6}	437.836
44	424.24×10^{-9}	134.40×10^{-6}	228345
45	427.36×10^{-9}	133.88×10^{-6}	20167.1
46	407.49×10^{-9}	127.31×10^{-6}	401634
47	409.68×10^{-9}	126.77×10^{-6}	31419.1
48	391.63×10^{-9}	120.89×10^{-6}	539593
49	392.97×10^{-9}	120.37×10^{-6}	39033.1

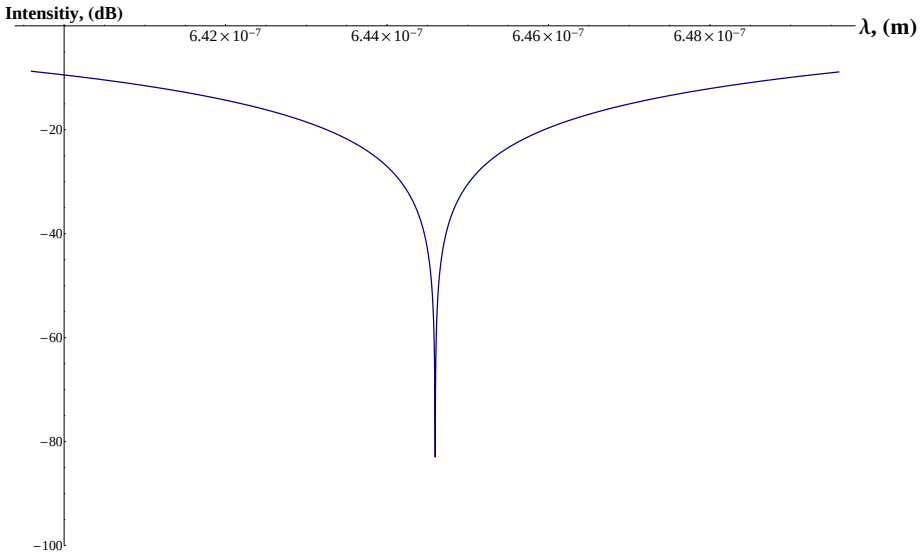

Figure 4.2: Absorption spectrum with a very short grating (24 periods), with the highest coupling strength and refractive index contrast

chosen for the modelling in Chapter 5, with a length of $L = 400\Lambda$ and refractive index contrast of $\sigma = 1.91 \times 10^{-4}$, results in spectrum shown in Figure 4.4. This also is the mode of interest that will be further discussed uncertainty analysis in Chapter 7.

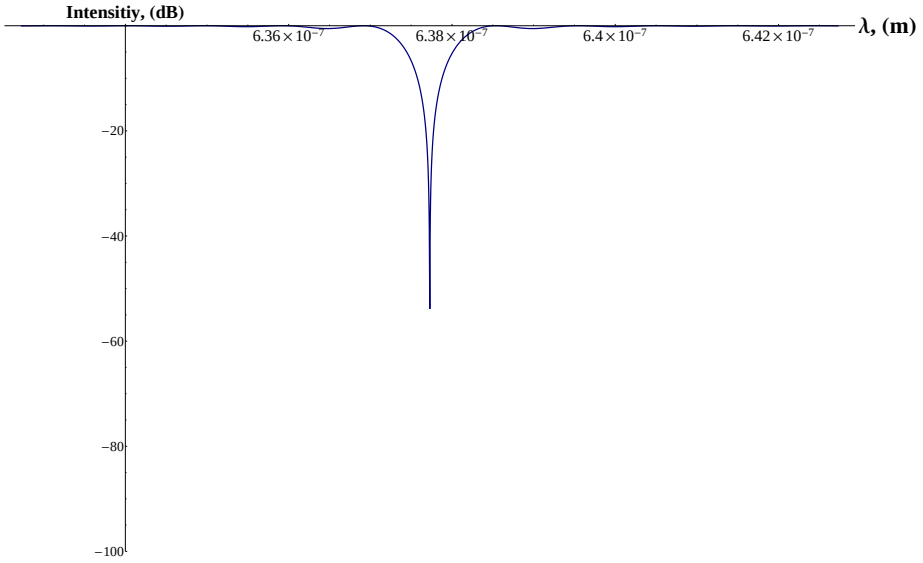

Figure 4.3: Absorption spectrum with a very long grating (1000 periods), with a low coupling strength

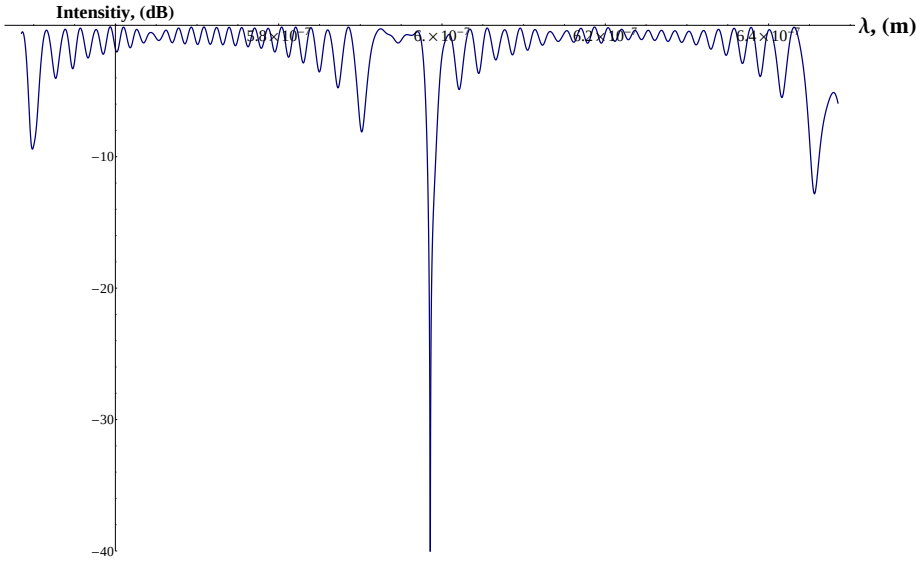

Figure 4.4: Absorption spectrum with the 31st mode, a long grating (400 periods, or about 8 cm), and the contributing effect of all other coupling modes also visible

4.3 Conclusion

This chapter has illustrated the solving the LPFG theory to find a set of solutions that are of interest for high sensitivity gratings. The fact that there are many solutions is actually beneficial, as there is choice regarding the coupling constants, enabling the choice of longer or shorter length LPFGs depending on the limitations of given design parameters. Additionally, as discussed in Chapter 8, specifically Eq. 8.1, there exists a set of LPFG solutions that are insensitive to temperature and would form a similar set of solutions to the high γ solutions. Having both sets could allow finding a highly sensitive LPFG that is immune to temperature changes, however this is not investigated

in this work, but is hopefully something that will be looked at in the future.

In Chapter 5, on designing a mandrel, a period grating 35 nm shorter is used than the periodicity of the turning point of the 31^{st} mode, as per Table 4.1. This gives a $\gamma \approx 6000$, and after taking into account elaso-optic properties defined in Eq. 3.56, gives a sensitivity of about 2000 nm/mϵ.

Chapter 5

Mandrel Theory

5.1 Introduction

Having established the theory for the Long Period Fibre Grating (LPFG) coupling modes and absorption spectra in the previous sections, it is necessary to extend the LPFG strain sensing model, to understand the spectral shift per Pascal.

There are several ways to convert pressure changes into strain on a fibre, but the most compact and well understand way is to wrap the fibre around a compliant mandrel. This chapter will closely follow the work of Pechstedt and Jackson (1995), which modelled a compliant mandrel as an accelerometer utilising phase changes. In contrast this approach will seek to design a pressure sensing mandrel, utilising frequency shifts.

5.2 Mandrel Sensitivity Theory

Pechstedt and Jackson (1995) defined the description of the compliant mandrel, which is slightly modified to calculate wavelength shift per strain, rather than phase shift as is the case for interferometric hydrophones.

Figure 5.1 illustrates the fibre wound compliant mandrel, where a is the inner radius of the mandrel, and can be zero; b is the outer mandrel radius; r z, and ϕ are the cylindrical radial distance, axial distance, and azimuthal angle defining any point on the mandrel; and L the length of the mandrel.

Pechstedt and Jackson (1995) establishes the strain tensor to be:

$$u_{\mathrm{ik}} = \begin{pmatrix} u_{\mathrm{rr}} = \alpha - \frac{\beta}{r^2} & 0 & 0 \\ 0 & u_{\theta\theta} = \alpha + \frac{\beta}{r^2} & 0 \\ 0 & 0 & u_{\mathrm{zz}} = \gamma \end{pmatrix} \tag{5.1}$$

With unknown constants α, β, γ. From Hooke's Law, the stress tensor is:

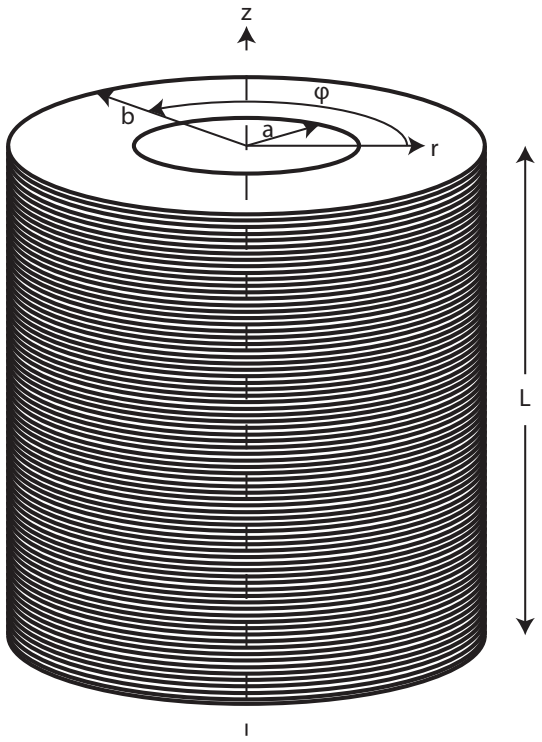

Figure 5.1: Illustration of the concept of a fibre wrapped mandrel, adapted from Pechstedt and Jackson (1995)

$$\sigma_{\mathrm{ik}} = \begin{pmatrix} \sigma_{\mathrm{rr}} = \frac{E}{1+\sigma}\left(\frac{\alpha+\sigma\gamma}{1-2\sigma} - \frac{\beta}{r^2}\right) & 0 & 0 \\ 0 & \sigma_{\theta\theta} = \frac{E}{1+\sigma}\left(\frac{\alpha+\sigma\gamma}{1-2\sigma} + \frac{\beta}{r^2}\right) & 0 \\ 0 & 0 & \sigma_{\mathrm{zz}} = \frac{E}{1+\sigma}\frac{\gamma(1-\sigma)+2\alpha\sigma}{1-2\sigma} \end{pmatrix} \tag{5.2}$$

Where E is the Young's Modulus of the mandrel, and σ is the Poisson ratio of the mandrel. It is assumed, in this treatment, that the pressure is only applied in the Z-direction on the mandrel.

$$p_z = \frac{F_z}{\pi\left(b^2 - a^2\right)} \tag{5.3}$$

Due to p_z a radial pressure p_r is generated acting on the surface of the cylinder towards the centre, to restore the shape of the mandrel. This leads to boundary conditions:

$$\begin{aligned} \sigma_{\mathrm{rr}} &= 0 \qquad @\ r = a \\ \sigma_{\mathrm{rr}} &= -p_r \qquad @\ r = b \\ \sigma_{\mathrm{zz}} &= -p_z \quad @\ z = 0, z = L \end{aligned} \tag{5.4}$$

The last of these boundary conditions indicates that pressure is acting on both ends of the mandrel at the same time. Pechstedt and Jackson (1995) models it in such a way because "the discussion is restricted to a quasi-equilibrium state", and goes on to point out that this treatment neglects the influence of stresses at the ends of the mandrel. This is a valid assumption since

the model is considering a thin mandrel, the pressure at both ends of the mandrel is likely to be approximately equal due to the near-instant stress propagation from one end of the mandrel to the other.

Taking end effects on the mandrel into fully account would create a very complicated model. At longitudinal distances larger than approximately the diameter of the mandrel, the strain distribution on the mandrel would suffer end effects, as per Saint-Venants principle. Modern discussions on the principle by Mises (1945) looks at to tackle this problem analytically, and states that Saint-Venants principle only really concerns long, thin rods. Since the compliant mandrel being considered here is assumed to be small and likely more disc shaped, end effects on the strain distribution should be small, as it will have its strain almost evenly distributed through its small body. So here Saint-Venants principle is neglected, in turn avoiding complicated finite element analysis to resolve second order effects.

Now in order to derive p_r, the fibre tension force F_t on the mandrel must be considered.

$$\sigma_{\mathrm{rr}} = \frac{F_t N}{bL} \tag{5.5}$$

Where N is the number of turns of the fibre around the mandrel, and F_t is the fibre tension. A small change to mandrel radius leads to a change in fibre tension and a hence a corresponding strain on the fibre:

$$\delta F_t = k_{\mathrm{fn}} \frac{\delta L_f}{L_f} = k_{\mathrm{fn}} \epsilon \tag{5.6}$$

Where L_f is the length of the optical fibre; ϵ is the strain on the cable; and k_{fn} is the normalised fibre stiffness:

$$k_{\mathrm{fn}} = E_f \ \pi \ {r_f}^2 \tag{5.7}$$

Where E_f is the Young's Modulus of the fibre; and r_f is the radius of the fibre. Now:

$$p_r = \frac{N}{bL} \left(k_{\mathrm{fn}} - F_t\right) \frac{\delta L_f}{L_f} = \frac{\left(k_{\mathrm{fn}} - F_t\right) N}{bL} \ \epsilon \tag{5.8}$$

Using the complete boundary conditions, the stress tensor (Eq. 5.2) can be solved to find α, β, γ:

$$\begin{gathered} \alpha = \tfrac{1}{E} \left(\sigma p_z + (1-\sigma) p_r \tfrac{b^2}{a^2-b^2}\right) \\ \beta = \tfrac{1}{E} (1+\sigma) p_r \tfrac{a^2 b^2}{a^2-b^2} \\ \gamma = \tfrac{1}{E} \left(p_z + 2\sigma p_r \tfrac{b^2}{a^2-b^2}\right) \end{gathered} \tag{5.9}$$

Allowing us to calculate the changes in Mandrel length and Fibre length:

$$\begin{gathered} \delta L = \int_0^L u_{zz} \, dz = \gamma L = \tfrac{L}{E} \left(p_z + 2\sigma p_r \tfrac{b^2}{a^2-b^2}\right) \\ \delta L_f = \int_0^{2\pi} u_{\theta\theta}(b) b \, d\theta = 2\pi b u_{\theta\theta}(b) = \tfrac{L_f}{E} \left(\sigma p_z + p_r \left(\sigma + \tfrac{a^2+b^2}{a^2-b^2}\right)\right) \end{gathered} \tag{5.10}$$

Now eliminating p_z gives:

$$\frac{\delta L_f}{L_f} = \epsilon = -\sigma \frac{\delta L}{L} \frac{1}{X} \tag{5.11}$$

Where,

$$X = 1 - \frac{k_{\text{fn}} N}{LEb}\left(\frac{b^2}{b^2 - a^2}\left(2\sigma^2 - 1\right) - \frac{a^2}{b^2 - a^2} + \sigma\right) \tag{5.12}$$

Lastly, in order to define the sensitivity of an accelerometer, the effective cylinder stiffness is defined by:

$$\delta L \; K_{\text{eff}} = -F_z = -p_z \pi \left(b^2 - a^2\right) \tag{5.13}$$

Where K_{eff} is the stiffness of the mandrel:

$$K_{\text{eff}} = \frac{E}{L}\pi\left(b^2 - a^2\right) + \frac{2\pi\sigma^2 k_{\text{fn}} N b}{L^2 X} \tag{5.14}$$

First term here is the contribution from the cylinder material, and the second term is due to the wrapped fibre. The second term is important for a compliant mandrel, since the wrapping fibre would effectively stiffen a mandrel.

Resonance frequency is defined as:

$$f_0 = \frac{1}{2\pi}\sqrt{\frac{K_{\text{eff}}}{m + \frac{m_{\text{cyl}}}{3}}} \tag{5.15}$$

This definition of resonance frequency by Pechstedt and Jackson (1995) relies on the fact that these is an external seismic mass, m, which has a large contribution to the resonant frequency. In the case of a very simple compliant mandrel that is considered here, m will ideally be zero since there will be no large mass attached to the mandrel, leaving the mass of the cylinder as the only contribution to the resonant frequency. In this scenario, the definition for the resonant frequency is a poor one, since it breaks the assumption of $m \gg m_{\text{cyl}}$ if no mass is implemented. An experimentally derived relationship for the resonant frequency is needed.

Having already defined LPFG sensitivity in Eq. 3.56, an expression for the wavelength shift vs. acceleration can be defined:

$$\left(\frac{\delta\lambda_D}{a_0}\right)_0 = \frac{\left(\frac{\partial\lambda_D}{\partial\epsilon}\right)\epsilon}{a_0} \tag{5.16}$$

Evaluating this using Eq. 5.11

$$\implies \left(\frac{\delta\lambda_D}{a_0}\right)_0 = \frac{\left(\frac{\partial\lambda_D}{\partial\epsilon}\right)\left(-\sigma\frac{\delta L}{L}\frac{1}{X}\right)}{a_0} \tag{5.17}$$

$$\implies \left(\frac{\delta\lambda_D}{a_0}\right)_0 = \frac{\left(\frac{\partial\lambda_D}{\partial\epsilon}\right)\left(-\sigma\frac{\left(\frac{a_0}{(2\pi f_0)^2}\right)}{L}\frac{1}{X}\right)}{a_0} \tag{5.18}$$

$$\implies \left(\frac{\delta\lambda_D}{a_0}\right)_0 = \frac{-\sigma\left(\frac{\partial\lambda_D}{\partial\epsilon}\right)}{LX\left(2\pi f_0\right)^2} \tag{5.19}$$

For the purposes of analysis, the equation for f_0 is substituted from Eq. 5.15, even though it is not a good estimate:

$$\left(\frac{\delta\lambda_D}{a_0}\right)_0 = \frac{-\sigma}{LXK_{\text{eff}}}\left(m + \frac{m_{\text{cyl}}}{3}\right)\frac{\partial\lambda_D}{\partial\epsilon} \tag{5.20}$$

$\left(\frac{\delta\lambda_D}{a_0}\right)_0$ is the constant that defines the wavelength sensitivity to acceleration applied on the mandrel in the Z-direction.

The sensitivity, with respect to signal frequency is as follows:

$$\frac{\delta\lambda_D}{a_0}(f) = \left(\frac{\delta\lambda_D}{a_0}\right)_0 \frac{{f_0}^2}{\sqrt{\left(f^2 - {f_0}^2\right)^2 + \left(\frac{f\times f_0}{Q}\right)^2}} \tag{5.21}$$

where Q is the quality factor of the mandrel (10 is typical in the work done by Pechstedt and Jackson (1995)), and f is the signal frequency.

However, it is desirable to treat the mandrel as a pressure sensor, deformable from all directions. Assuming the mandrel is compliant, deformations from all sides of the mandrel would create strains on the fibre that is wound around it, and would all be detectable. However, here the analysis is restricted to pressure applied to one end of the mandrel in the Z-direction, because it greatly simplifies the ability to estimate sensitivity, however the result will be a considerable underestimate of real sensitivity.

Here, the top of the mandrel is treated as the only surface which has a pressure applied to it, to keep the model simple. Pressure, P, is defined as:

$$P = \frac{F}{A}, \tag{5.22}$$

where F is the force applied, and A is the area. In the mandrel, the area in question will be defined as:

$$A = \pi\left(b^2 - a^2\right) \tag{5.23}$$

While F will be mass times acceleration. Because measuring the sensitivity in Pascals (Pa or kg/m^2) is desirable, the acceleration defined by Eq. 5.20, can be written to give a wavelength shift per unit Pa, which can be converted in the absorption frequency shift per Pa. In other words:

$$\frac{\delta\lambda_D}{P_0}(f) = \left(\frac{\delta\lambda_D}{P_0}\right)_0 \frac{{f_0}^2}{\sqrt{\left(f^2 - {f_0}^2\right)^2 + \left(\frac{f\times f_0}{Q}\right)^2}} \tag{5.24}$$

with,

$$\left(\frac{\delta\lambda_D}{P_0}\right)_0 = \pi\left(b^2 - a^2\right)\left(\frac{\delta\lambda_D}{a_0}\right)_0 \tag{5.25}$$

is the wavelength shift, in meters, per Pascal.

This is clearly an underestimate of the pressure applied to a highly compliant mandrel, but without experimental work and a better definition of f_0 this is a good enough approximation for analytical purposes.

5.3 Design Specifications

In the design of the mandrel, the first assumption is that the fibre wound be tightly would along the entire length of the cylinder (L). However, the length of the LPGF, is much shorter than a tightly fibre around a mandrel of radius 5 mm, and length $L = 1.2\ r$. This model draws upon the results from Waagaard et al. (2001) and maintains a mandrel Length to radius ratio of 1.2, giving ideal pressure-to-acceleration responsiveness.

Active fibre should be wound to cover as much of the length of the cylinder, such that it can deform under any non-uniform strain variations within the mandrel. The rest of the mandrel would need to be wound with other fibres of similar coiling tension such that the cylinder would have the stiffness of the fibre acting on its whole length.

It is equivalent to treat the fibre wrapping the cylinder as a single fibre of sufficiently large L_f, such that the fibre is wound tightly with no gaps from top to bottom, where only a small section of the fibre has the LPFG inscribed. Such an arrangement will strictly look at circumference changes of the around the centre of the mandrel where the LPFG is inscribed, and will hence be vulnerable to noise generated by end effects due to Saint-Venants principle.

Given the equation for a helically wound fibre of radius r_f of length L_f, wound N times around a cylinder of radius r, with length 1.2 r, the length of the fibre follows equality:

$$L_f = \sqrt{(r + r_f)^{\,2} + \left(\frac{1.2\ r}{N}\right)^2}\ 2\pi N \tag{5.26}$$

where N is the number of turns the fibre makes around the mandrel. If the mandrel is tightly wound, this would be equivalent to:

$$N = \frac{L}{2r_f} \tag{5.27}$$

$$\implies N = \frac{1.2r}{2r_f} \tag{5.28}$$

The mass of the cylinder is assumed to include the mass of the fibre that is wound around it, since the cylinder will be very small and light, the mass added by wrapping fibre mass will not be a negligible contribution to resonant properties of the cylinder. So:

$$m_{\text{cyl}} = \pi \left(b^2 - a^2\right) L\ \rho + m_f\ L_f \tag{5.29}$$

Where ρ is the density of the cylinder, and m_f is the mass of the fibre per metre. The mass of the fibre is estimated at 194 g/km (W. White, Chromis Fibreptics, Personal Communication, 3$^{\text{rd}}$ April 2014).

Lastly, no inner radius is assumed. Inner radius would improve sensitivity due to requiring added external mass to maintain the area exposed to pressure change, and also prevent water from entering the centre of the cylinder, which would be detrimental to the sensor's ability to experience deformations from directions other than the Z-direction. Section 5.4.1 looks at the case of adding a zero mass cover to an air-backed mandrel, illustrating loss of sensitivity of a compliant mandrel with an inner radius.

5.4 Predicted Operating Specifications

Fibre specifications for modelling will follow to work of Silva-Lpez et al. (2005), which states all the relevant information regarding Polymethyl Methacrylate (PMMA) fibre, which is an ideal fibre for the purpose of this sensor. The mandrel specifications (Roylance, 1999) of Polyurethane provide the rest of the information needed to solve the sensitivity equation, using numerical modelling from the previous sections and Silva-Lpez et al. (2005) to provide the LPFG resonant wavelength to stain sensitivity. Other mandrel materials for example, Polybutadiene is even more compliant than Polyurethane, but could be damaged at higher pressures. All of this information, and its origin is summarised in Table 5.1.

Table 5.1: Summary variables contributing to the Mandrel

Variable	Value Used	Reference
Q (mandrel quality factor)	10	Pechstedt and Jackson (1995)
F_t(coiling tension)	$1.1N$	Pechstedt and Jackson (1995)
r_f (fibre radius)	62.5 μm	Silva-Lpez et al. (2005)
R (outer mandrel radius)	5000 μm	Roylance (1999)
a (inner mandrel radius)	0 μm	Desired value
ρ (mandrel density)	1200 kg/mˆ3	Roylance (1999)
m_f (fibre mass)	0.194 g/m	Personal Contact
m (seismic mass)	0 kg	Desired value
E (mandrel Young's Modulus)	0.025×10^9Pa	Roylance (1999)
E_f (fibre Young's Modulus)	2.8×10^9Pa	Silva-Lpez et al. (2005)
σ (mandrel Poisson Ratio)	0.5	Roylance (1999)
μ (fibre Poisson Ratio)	0.34	Silva-Lpez et al. (2005)
p_{11},p_{12} (strain optic coefficients)	$0.300, 0.297$	Silva-Lpez et al. (2005)
λ_D (resonant wavelength)	598.5 nm	Mode 31
γ (strain sensitivity constant)	6170.8	Mode 31
n_1 (fibre refractive index,core)	1.4923	Silva-Lpez et al. (2005)
n_2 (fibre refractive index,cladding)	1.4905	Silva-Lpez et al. (2005)
n_{effco} (effective index,core)	1.4914118992	Mode 31
n_{effcl} (effective index,cladding)	1.4886405100	Mode 31

Using the discussed theoretical and numerical treatment of the wound mandrel, the resonant frequency shift resulting from pressure variations on the mandrel is modelled across range of acoustic frequencies. Figure 5.2 is a plot of the response, in terms of sensor frequency shift with respect to acoustic frequency.

The plot in Fig. 5.2 shows the frequency shift of the resonant peak to be 3.205×10^6 Hz shift per Pascal (roughly 0.1 pm/Pa centred on 598.5 nm). The detectability of such a shift is discussed in the Chapter 6, which discusses the experimental set-up and sensitivity of a heterodyne. To give this sensitivity more meaning, using a typical air-gun in marine acquisition, firing a 10 MPa wave, spherically expanded from a refection at 3 km down, to a receiver (i.e. this instrument) 5 km horizontally from the source would need to be able to resolve 0.23 Pa Pa of pressure change. Heterodyne techniques conceptually similar to what is considered in Chapter 6 applied in Lu et al. (2015), while using a low speed photodetector, resolve shifts as low as 10 kHz with an accuracy of about 60 Hz. Being able to discriminate 70 kHz shifts on a sensitivity of 3 MHz/Pa, gives precise recovery of pressure changes as low as 0.023 Pa. This suggests that the sensitivity goal that is

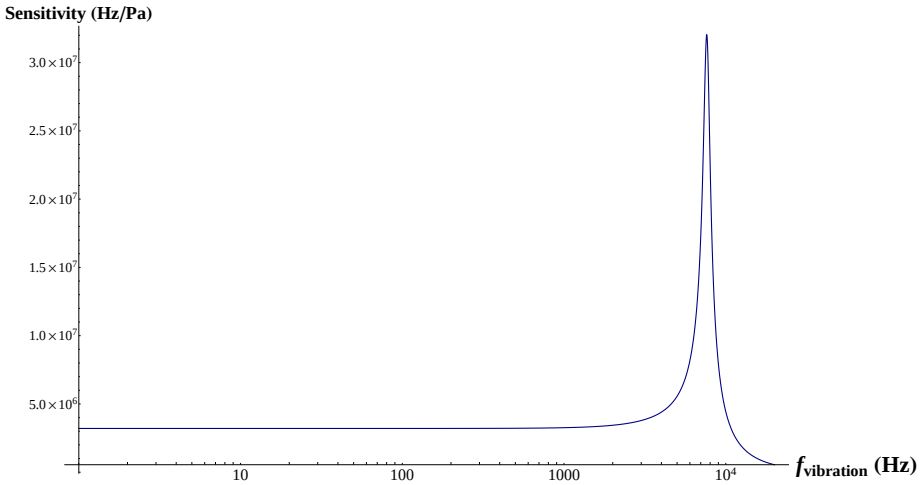

Figure 5.2: Sensitivity of the mandrel with respect to frequency of incoming pressure signal

being set is sensible. The work of Lu et al. (2015) comfortably achieves a resolution 1000 times what is required, however the case considered there is a different in that they use a low-speed photodetector, which is much more accurate, and optical bandwidth of their signal is significantly narrower. Proving that reliably discriminating 70 kHz shifts for the LPFG design requires an experimental set-up to be able to test the impact of various noise factors that would influence the resolution.

Another thing to point out is the strain sensitivity of the fibre itself, being roughly 2000 nm/mϵ. This is much higher than most LPFG, because it has been specifically designed to operate on a highly sensitive mode. If sensitivity this high cannot be achieved in the LPFG (Chapter 7), increasing the radius (and thus Length) of the mandrel will be able to increase the sensitivity, but this is undesirable since the aim is to design a compact sensor. Also experimental construction of this mandrel should exhibit higher pressure sensitivity than what is calculated here, since the model uses very simple uni-axial pressure applied only to one end of the mandrel.

5.4.1 Air-backed Mandrel

Mandrels for hydrophones are typically designed with air backing to improve their sensitivity.

Modelling done in the code (MandrelEval.nb) for the case of the very small compliant mandrel, is illustrated by Figure 5.3 showing an air-backed compliant mandrel reduces in sensitivity as an inner radius is introduced. The model used assumed that some sort of cap was placed on the small compliant mandrel, to maintain the same effective area exposed to pressure changes. This actually introduces a non-zero seismic mass to the function that is not accounted for, but when modifying this mass in the code, shows that the total sensitivity would improve greatly, and would still peak at inner radius $a = 0$, but reduces the resonance frequency.

5.5 Conclusion

There are many varieties of plastic fibre available, and the choice of PMMA, while ideal for modelling due to having a similar structure to regular silicon fibre, is not final, and the choice will depend on

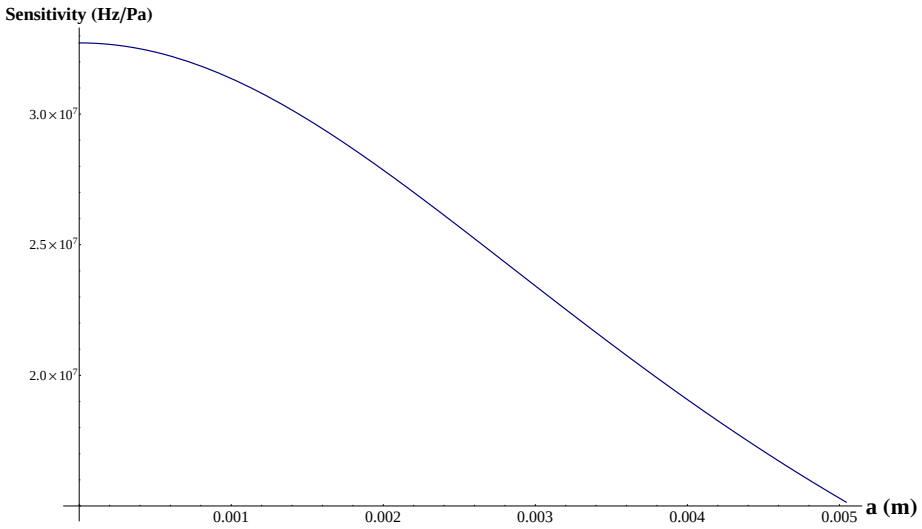

Figure 5.3: Sensitivity of the mandrel compared to changes in inner radius, a

many variables such as cost, availability, and manufacturing issues concerning LPFGs. Additionally inscribing the LPFG into a PMMA fibre will almost certainly require diameter modulation (See Appendix A), and how that fibre conforms to the theory presented here needs to be tested.

Alternative mandrel materials can also be considered. For example, Polybutadiene is even more compliant than Polyurethane, but is more fragile.

Sensitivity characteristics can be improved with larger mandrel geometries, potentially offsetting detrimental effects of LPFGs which have lower strain sensitivity. Decisions concerning this will come from experience with the physical construction with the instrument, as well as the costs.

Lastly, some experimental work needs to be done to fully understand the resonant frequency of a small, zero-seismic mass, mandrel of arbitrary geometry; whether the mass of the wrapping fibre has a significant impact; as well as bending effects on the fibre, i.e. birefringence effects.

Chapter 6

Proposed System Design

6.1 Introduction

Having considered the design of the Long Period Fibre Grating (LPFG) frequency domain sensor it is necessary to consider how to observe the shift. A simple heterodyne arrangement should be able to isolate the signal and shift it to a part of the frequency spectrum which is less noisy, and be able to sample it at fast rates limited only by a photodetector. This chapter is dedicated to what must be considered when constructing a heterodyne to isolate the pressure sensitive signal, with the main issue being that LPFG absorption notches are spectrally broad, and heterodyne arrangements have Signal to Noise Ratio issues when used with broad intermediate filters.

Chapter 4 has modelled that with good LPFG construction, the line-width is expected to be about 1 nm, centred on about 598.5 nm, meaning it is almost 1 THz wide. It is expected that, when experimentally investigated, this line-width will prove to be much too broad, and a much longer LPFG will be required to make it narrower, at the cost of creating strong neighbouring fringes which will need to be accounted for in the signal processing.

Lets consider the shift generated by the LPFG considered previously, about 3 MHz/Pa. Crudely speaking, ability to detect a shift of within a resolution of 70 kHz with a sensitivity of 3 MHz/Pa, means pressure variations on the order of 0.023 Pa can be discerned. Lu et al. (2015) gives a promising indication that this is possible, but as always this is an aspect that needs experimental confirmation. Considering the pressure observable due to a 10 MPa air-gun array from sensor 5 km away after a reflection from 3 km down (assuming spherical wave-front spreading) results in a pressure change of 0.23 Pa, the sensitivity of the sensor considered so far would be sufficient.

There are several complications to consider in the proposed design of a hydrophone utilising a LPFG, or Varying waveLength Acoustic Detector (VLAD), and this chapter will serve to highlight what they are and how they can be tackled experimentally. Ideally the conclusion of this chapter could server as a starting experimental design for future research.

6.2 Signal Spectrum

Chapter 4 demonstrated the expected absorption spectrum of the desired LPFG construction (Figure 4.4), taking into account all of the cladding mode interference interactions at and around the

a predetermined wavelength of interest. As illustrated the resonant absorption line is significantly narrower and stronger than nearby interference fringes caused by other cladding modes.

This was modelled using polymethyl methacrylate (PMMA) (Silva-Lpez et al., 2005) fibre, since at the time of writing full information concerning strain-optic coefficients as well as Young's Modulus and Poisson Ratio of other plastic fibres is not published. The reason plastic, or PMMA, fibre is desirable is that it can potentially conform to a very tight minimum bend radius of 5 mm, which would allow for very compact sensors. Also PMMA fibre can be made as a single mode step index fibre, rather than multi-mode graded-index like most plastic fibres, meaning that no further assumptions needed to be made concerning LPFG theory which was set down by Erdogan (1997a).

However, the existing model for the LPFG absorption spectrum is incomplete. Since the optic fibre is ideally going to be wound tightly around a mandrel of minimum radius, it is necessary to take into account effects from bending and birefringence. Block et al. (2006) discusses bending of LPFGs creating resonance mode splitting in detail. Bending creates birefringence inside the fibre, where the two polarisation states of the source light split and become degenerate. What is concerning is that bending of radius of 25 cm, in the work by Allsop et al. (2004), is already splitting a resonance mode into two, separated by about 45 nm. Block et al. (2006) and Allsop et al. (2004) provide linear models for the mode splitting, however it is the intention of this work that the LPFG be wound tightly around a mandrel of radius 5 mm, and since previous work only considered silicon fibres, such tight bend radii have not been considered and models cannot be extrapolated to such an extremely tight radius. This means that to get a meaningful implementation of a tightly wound LPFG, careful experimental analysis would need to be conducted to understand how to best work around, or make use of, bending effects. Unfortunately this is beyond the scope of this thesis.

One way to mitigate birefringence problems is to polarise the light, before it enters the LPFG or a bent fibre section, at a 45°angle to the bending, such that the fibre has minimum bending sensitivity (Wang et al., 2007). It is expected that the observed resonance mode will appear like Figure 4.4, with no mode splitting occurring.

On the other hand, the bent LPFG in Allsop et al. (2004) showed different temperature sensitivity and Chiavaioli et al. (2013) demonstrates external refractive index sensitivity improvements. A spectral model (Gonzalez et al., 2001) exists and could be used to model spectral changes as a function of birefringence, but not for very tightly bent fibres. As seen in Shu et al. (2002), temperature, external refractive index and strain sensitivity are all partially related by the γ term, implying that improvements in strain sensitivity of one of the degenerate modes in a bent fibre would be observable. Rather than polarising the light as a work around birefringence issues, polarising the light before it enters the LPFG in an orientation that would pick out a more strain sensitive degenerate birefringent mode could improve the sensitivity of the detector, and is a topic for further experimental research.

This signal spectrum itself is a transmission dip, rather than the emission peak that is usually used in a heterodyne. This presents the extra challenge that needs to be experimentally solved. Conceptually, destructively mixing the signal with the unchanged source from the pump should leave the component of the transmission dip from the signal as the only remaining component. This has been considered in the optical circuit diagram and is illustrated by the implementation of variable phase controllers (VPC) that allow fine tuning the phase to get the most out of the desired destructive interference, though something more fancy would be required to ensure that all

frequency components from a broad range could cancel out.

6.3 Source Spectrum

The main concern of the heterodyne arrangement is to recover the difference in positions of the transmission dips between a reference source spectrum and the signal spectrum as quickly as possible, enabling time-domain multiplexed (TDM) arrays of as many detectors as possible, through means of a pulsed laser source. Lin et al. (2012) have experimentally demonstrated TDM LPFGs. It is worth noting that since the detectors have a short active fibre length there would be negligible change in phase, there is potential for using phase division multiplexing (PDM) (Leonard and Cimini, 1989). In combination with TDM, hopefully arrays large enough for seismic acquisition applications can be made. At the moment multiplexing schemes will not be discussed further, until a more complete understanding of such complications for final instrument is presented, likely after a prototype.

The source spectrum is an important consideration for the speed and bandwidth of the heterodyne. Because the signal output and the mixing source need to be coherent for ideal signal to noise ratio (SNR) (Protopopov, 2009), the best practice is to mix the signal with a source that has the same spectral profile. Generating a broad source spanning 1 THz is possible using super-continuum generation (Dudley and Taylor, 2010, Chapter 8). For a heterodyne arrangement to function, the source used for mixing with the signal is typically freuqnecy shifted using an Acousto-Optic Modulator (AOM). This moves the mixed heterodyne signal to an intermediate frequency (IF), defined by the frequency of the AOM. With an IF shift it is easy to isolate the signal of interest with a bandpass filter, leaving only the mixed signal centred on the IF frequency which can analysed by electronic devices, using a lock-in amplifier. This is the most attractive aspect to the heterodyne arrangement, as it isolates the signal allowing for observation of frequency shifts in the signal.

There are some complications with this arrangement. To be able to observe frequency shifting of up to several Pascals, a sufficiently broad optical source is needed. Broad-band photodetectors have short data collection times (Bingham et al., 1998) ($\Delta\nu = \frac{1}{2\tau}$, τ is the data collection time), which is relevant for TDM of the instrument, because a short data collection time means that less light will be collected by photodetectors, meaning the system will be more prone to noise. This is thankfully not an issue here since the power of the signal arm of the heterodyne will be comparable and arbitrarily large compared to the source. Additional problems arise from using an AOM with a broad source, as the AOM will not preserve the spectrum due to diffraction angle dependence on wavelength, which will create distortions in the shifted spectrum adding noise to the mixed signal, but with the use of a spherical mirror this can be compensated for (Hirai, 2001; Matsumoto and Hirai, 1999), improving SNR. This is however a very fragile arrangement that may work in a laboratory, but will not be practical for field use.

Lastly, the final design should modify the source spectrum with a reference LPFG with a static absorption frequency, which should help resolving the signal frequency shift. The heterodyne will be very good at resolving the shifts in two similar spectral profiles. Regardless, this would need to be experimentally demonstrated.

6.4 Heterodyne Signal to Noise Ratio

In a heterodyne, the signal to noise ratio, Q, is defined as (Protopopov, 2009, Chapter 1.3):

$$SNR = Q = \frac{\text{Signal Strength}}{\text{Shot noise + Thermal Noise}} \tag{6.1}$$

$$Q = \frac{2\left(\frac{\eta q}{h\nu}\right)^2 P_1 P_2 R}{2qR\left(\frac{\eta q}{h\nu}\left(P_1 + P_2 + P_B\right) + j_D\right)\Delta\nu + 4kT_R F'\,\Delta\nu} \tag{6.2}$$

Where η is the quantum efficiency of the photo-detector; R is the active payload resistor of the photo-detector, depending on its electrical circuit; q is the electron charge; $h\nu$ is the mean photon energy of the interfering waves; P_1, P_2, P_B are the effective values of power for the signal, source, and background radiation incident on the photodetector; $\Delta\nu$ is the spectral width of the intermediate frequency (IF) bandpass filter; and j_D is the photodetector dark current. If neglecting thermal noise with a strong source (P_2), then R does not affect the signal to noise ratio, but η does. η is typically higher in more expensive photo-detectors, and if a final design would require a balanced heterodyne receiver, with two photo-detectors, the cost would be very significant. Since the product of P_1 (signal) and P_2 (reference source) is going to be very large (reduced only be Rayleigh scattering in the longer signal arm), the mixed signal strength will be strong and correspondingly the SNR will be large. However the spectral width of the IF bandpass filter, $\Delta\nu$, will be large due to the need to capture a broad spectrum. $\Delta\nu$ will be a product of the required dynamic range of the pressure sensor, in Pascals, and the frequency shift per Pascal. Reducing sensitivity of the sensor would help reduce the width of the IF filter, at the cost of sensor precision. Alternatively $\Delta\nu$ can be narrowed down to look at only one slope of the LPFG notch - such that the SNR improves.

Typically heterodyne systems can cope with very weak signals (i.e. $P_2 \gg P_1, P_B$), in cases with a narrow IF filter. This less relevant for this LPFG design, but highly applicable to Rayleigh backscattering techniques. In these situations, with strong enough source power, the signal to noise ratio approaches:

$$Q = \frac{\eta P_1}{h\nu\ \Delta\nu} \tag{6.3}$$

This illustrates that it will be difficult to use a broad IF filter in such situations, since $\Delta\nu$ will be large, which is why Rayleigh backscattering techniques often involve complicated cross-correlation algorithms.

6.5 Proposed Arrangement

Taking into account the discussed considerations required to build a functioning heterodyne detection scheme, below is a schematic diagram for the final deign of VLAD:

In Figure 6.1 BBS is the broad-band source, BS is a beam-splitter, PC is Polarisation Control, PD is a photo-detector, VPC is a variable phase controller, and dashed lines indicate electrical signals, while solid lines indicate optical signals.

A balanced arrangement would also help reduce noise from the reference arm, mitigating high-frequency variations and industrial noise, however it is more costly to set up, and adds a complexity with the extra beam-splitter, that could affect reliability. A balanced heterodyne receiver would

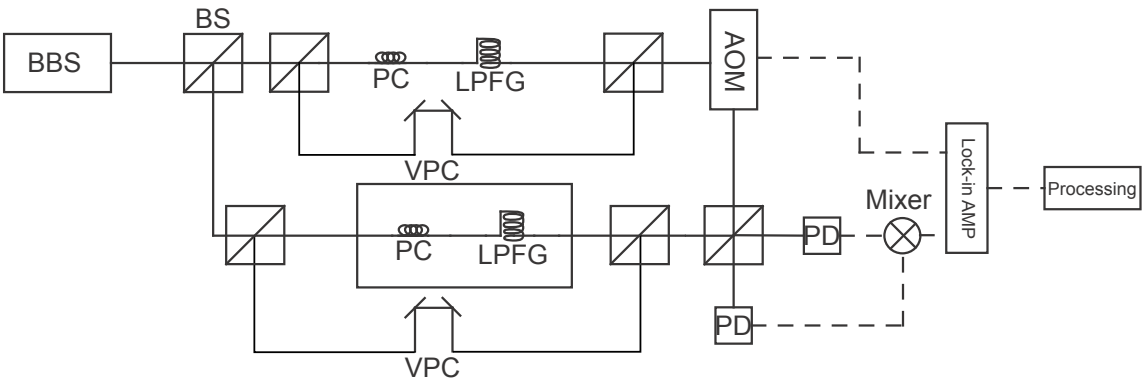

Figure 6.1: Circuit diagram of proposed balanced heterodyne arrangement

allow the direct discrimination of phase information from the signals, where PDM could be applied by using a variable phase control added to detectors arranged in parallel.

The AOM should be driven at a frequency sufficiently high as to isolate the signal at a high enough IF to be able to filter out the broad-band signal, but as low as possible to maximise the SNR. This would occur at frequencies higher than the bandwidth of the source laser. Hence careful choice of BBS bandwidth, AOM driving frequency, and IF filter bandwidth is required.

6.6 Conclusion

This chapter discusses the design of an optical pressure sensor, VLAD, utilising LPFG's strong resonance shift due to strain. It benefits from having a strong signal due to a very strong absorption; good noise characteristics, limited only by shot noise; and having a small active sensing length, allowing for compact construction, and phase division multiplexing.

A careful study of tight bending effects of LPFG, using plastic or PMMA fibres, will serve to better understand, and take advantage of, previously uncharacterised changes to strain sensitivity of LPFGs in tightly wound scenarios. This, in combination with a prototype construction of the VLAD for Down-Hole pressure sensing, is expected to be a good point of future work.

Chapter 7

Uncertainty Analysis

7.1 Forward Uncertainty Propagation Analysis

7.1.1 Introduction

For each variable used when calculating the final sensor sensitivity, there is a certain tolerance associated with its value due to finite precision of their measurement. These tolerances need to be propagated to give us an understanding of the uncertainty that is associated with the sensor. When designing number of sensors that all need to perform similarly, a guarantee of repeatability in the manufacture of the LPFG is required. Manufacturers of optical fibre publish data sheets with the values and for most details of their fibre, however characteristics of fibres important for LPFGs are rarely published, let alone details on their tolerances.

This chapter seeks to illustrate what significance tolerances concerning the fibre have on the uncertainty in desired sensitivity and absorption bandwidth of a LPFG. It is important to understand whether a LPFG with a desired sensitivity discussed in previous chapters can be reliably manufactured. To do so, uncertainty propagation is performed through the equations published in Erdogan (1997a) and Shu et al. (2002), using analytical and Monte Carlo methods discussed in Bevington and Robinson (2003, Chapter 4). The analytical approach was used wherever possible, due to the large amounts of time required to numerically evaluate cladding modes of LPFGs using a Monte Carlo approach. The estimated propagation of uncertainty equation is:

$$\sigma_z{}^2 = \sum_j \left[\left(\frac{\partial z}{\partial v_j} \right)^2 \left(\sigma_{v_j} \right)^2 \right], \tag{7.1}$$

where σ_z is the standard deviation in function z, v_j is the j^{th} dependant variable of z, and σ_{v_j} is the standard deviation of each variable v_j.

In cases where this method is not applicable, Monte Carlo methods were utilised to ascertain the uncertainty. Uncertainty is investigated using a model of the PMMA single mode fibre, coupling near the turning point of the 31^{st} mode, which has been the point of discussion in previous chapters.

LPFG strain sensitivity uncertainty is modelled using variables that describe fibres that have been published in previous works and in data sheets. The model uses published and commercially advertised uncertainties in: LPFG periodicity, Λ; core radius, a_1, and refractive index, n_1; cladding

radius, a_2, and refractive index, n_2; fibre Poisson Ratio, μ; and elasto-optic coefficients p_{11}, p_{12}, of a PMMA single mode fibre described in Silva-Lpez et al. (2005). Uncertainties in the laser wavelength and power, while they will be neglected in this work, have consequences for the effective refractive indices, n_{effco} and n_{effcl}, LPFG sensitivity, as well as the coupling constant, κ. Lasers with good frequency and power stability have existed for some time (Morkel et al., 1990), and as a result play a far less significant role than the geometric uncertainties of a optical fibre, and as such they are deemed negligible. Concerning the wavelength dependence on refractive index, the wavelength used in the underlying work described here is similar to that of Silva-Lpez et al. (2005) (35 nm difference). Consequently, wavelength dependence on refractive index is neglected, as well as any associated uncertainties. In all cases the stated uncertainty is assumed to be the standard deviation around the mean value in a Gaussian distribution.

7.1.2 Uncertainty in calculating LPFG coupling and sensitivity

Evaluation of uncertainty was done in LPFGuncertainty.nb. In this file under the heading of "Prep" is the symbolic evaluation of every uncertainty concerning a LPFG, except for the uncertainty in κ, which gets evaluated in memory as the symbolic evaluation in terms of a_1, a_2,n_1 and n_2 comes to almost 80 megabytes of text and effectively cripples the analysis.

The uncertainty in the most critical equations describing the sensitivity (Eq. 3.56) and the coupling strength, κ (Eq. 3.42) rely entirely on the tolerances in the geometric, refractive and elasto-optic properties of the fibre. In the case of sensitivity, the tolerance in the period grating, Λ, is also important. Table 7.1 is a summary of the figures that can be collated from literature and optical fibre data sheets.

Uncertainties are best stated as a fraction of the uncertainty of a value over the actual value, $\frac{\sigma_z}{z}$, to best be able to quickly discern the magnitude of the uncertainty for the variable.

Table 7.1: Summary of initial constant tolerances

Variable	Value (z)	Uncertainty (σ_z)	$\frac{\sigma_z}{z}$	Reference
a_1	3 μm	1.2×10^{-1} μm	4.00×10^{-2}	Silva-Lpez et al. (2005); Welker (2014)
a_2	62.5 μm	2.0×10^{-1} μm	3.20×10^{-3}	Silva-Lpez et al. (2005); Draka (2010)
n_1	1.4923	5.0×10^{-5}	3.35×10^{-5}	Silva-Lpez et al. (2005)
n_2	1.4905	5.0×10^{-5}	3.35×10^{-5}	Silva-Lpez et al. (2005); Waxler et al. (1979)
μ	0.345	5.0×10^{-4}	1.45×10^{-3}	Raftopoulos et al. (1976)
p_{11}	0.300	6.0×10^{-3}	2.00×10^{-2}	Waxler et al. (1979)
p_{12}	0.297	5.94×10^{-3}	2.00×10^{-2}	Waxler et al. (1979)
Λ	216.053 μm	4.00×10^{-2} μm	1.85×10^{-4}	Sugitatsu et al. (2001)

Table 7.1, illustrates the tolerances in the initial constants describing the optical fibre and period grating, that have been used in the propagation of uncertainties that follow. Tolerance for a_1 having a value of 4% is sourced from personal communication with manufacturer 'Paradigm Optics' (Welker, 2014), stating radius uncertainties of this cable to be between 2% to 4%. In regard to the Poisson ratio, μ, tolerance is assumed to be within the last decimal place. Lastly, the value of the LPFG grating periodicity, Λ, is such that a sensitivity of roughly 2000 nm/mϵ is achieved, which corresponds to the sensitivity discussed in the previous sections. Uncertainty in Λ

is theoretically lower, since uncertainties of 2.5 nm in the fabrication of Fibre Bragg Gratings are possible Chung et al. (2011).

Data-sheets regarding other commercial fibres cite tolerance in the cladding radius, a_2, to be as low as or $2.0 \times 10^{-1} \mu m$, (Draka, 2010) for silicon fibres. This has a significant impact on the LPFG uncertainty, as it improves certainty in the cladding mode propagation. For the purposes of investigating uncertainty propagation the value of $2.0 \times 10^{-1} \mu m$ is used to evaluate LPFG uncertainty, rather than the 4% tolerance.

Uncertainty in the refractive index contrast, σ, is estimated from the data in Kim et al. (2002), to be 1.56×10^{-5}, though only four data points were provided. This equates to roughly 10% of the σ value stated in Section 4, which was $\sigma = 1.91 \times 10^{-4}$. This is barely acceptable, but it should be reiterated that uncertainty in κ degrades the knowledge of what σ value is needed to create ideal bandwidth LPFG, and this section illustrates that there are significant issues with the uncertainty in κ.

Table 7.2 shows uncertainties on some of the most critical variables that control the uncertainty in sensitivity and κ, and have been propagated from the initial variable tolerances.

Table 7.2: Summary of Intermediate uncertainties

Variable	Value	Uncertainty	$\frac{\sigma_z}{z}$
n_{effco}	1.49141	6.06×10^{-5}	4.06×10^{-5}
n_{effcl}	1.48864	5.67×10^{-5}	3.81×10^{-5}
Δn_{eff}	2.77×10^{-3}	8.30×10^{-5}	2.99×10^{-2}
γ	5955.54	1.06×10^{6}	1.78×10^{2}
${E_{1\nu}}^{cl}$	1.36736	3.09345	2.26235

Looking at some intermediate uncertainties in Table 7.2, it is immediately clear that there will be issues with the final uncertainties. Uncertainty in $\Delta n_{\text{eff}} = n_{\text{effco}} - n_{\text{effcl}}$ rises significantly as a proportion of its value (compared to either n_{effco} or n_{effcl}), due to it being the difference in two similar values. This goes on to have a significant effect on the uncertainty in γ, as γ (Eq. 3.58, used in calculating strain sensitivity in Eq. 3.56) relates the reciprocal of the product of two small values, Δn_{eff} and Λ.

The significance of the uncertainty in $E_{1\nu}^{cl}$ is clear from Eq. 3.42. However the cause for this uncertainty is non-trivial to evaluate, and it is more informative to look at the uncertainty contribution to κ directly from all independent sources or uncertainty (namely a_1, a_2,n_1 and n_2).

It is already clear that geometric tolerances will dominated the uncertainties concerning the LPFG, and the uncertainty in the precision of the inscription is not a factor for concern.

Table 7.3: Summary of Resulting uncertainties

Variable	Value	Uncertainty	$\frac{\sigma_z}{z}$
λ_D	598.8 nm	0.18 nm	3.00×10^{-4}
κ	9.54×10^{4}	3.19×10^{6}	3.34×10^{1}
$\frac{d\lambda_D}{d\epsilon}$	1980 $nm/m\epsilon$	353000 $nm/m\epsilon$	1.78×10^{2}

Uncertainty in $\frac{d\lambda_D}{d\epsilon}$ is effectively entirely due to uncertainty in γ. Meanwhile, as evidenced

by comparing Table 7.3 and Table 7.2, $E_{1\nu}^{cl}$ is a significant contributor to the uncertainty in κ, but there are other large contributions. Independent contributions to the uncertainty of κ can be calculated. The precise evaluation is as follows:

$$\sigma_\kappa = \sqrt{1.783 \times 10^{10} + 9.784 \times 10^{12} + 3.696 \times 10^{11} + 5.728 \times 10^{11}}, \tag{7.2}$$

for arguments that represent sources of uncertainty from n_1, n_2, a_1 and a_2 respectively. It is clear here, that the largest source of error was the tolerance in n_2, as the uncertainty in the optical power distribution ($E_{1\nu}^{cl}$) is likely to also be strongly influenced by it. In theory, even if the only source of uncertainty was the tolerance of n_1, the uncertainty in κ would still be greater than the value of κ! As touched on in Section 6.1, it is expected that the bandwidth created by the ideal bandwidth is too broad and that having the LPFG be of much longer length is required. Having a much longer LPFG will invariably make the transmission dip of interest narrower hopefully to the point where having such great uncertainty in κ will not be detrimental to the outcome of the instrument.

From these issues it is clear that finding what tolerances are required for the initial values, such that the final LPFG uncertainties in κ and sensitivity are reasonable. This is a non-trivial and informative task that is addressed in Section 7.2.

7.1.3 Uncertainty in calculating Mandrel Sensitivity

So far issues arising from the construction of a LPFG have been looked at, which is unbent, and in a state of quasi-static stress. Winding and bending the LPFG around a mandrel introduces new problems, such as fibre birefringence. Birefringence is well beyond the scope of this uncertainty modelling, as there are significant issues in the uncertainty of the LPFG already. To be able to say something informative on the topic of uncertainty contributions in final sensitivity due to properties of the Polyurethane mandrel it is necessary to consider the theoretical scenario where the uncertainty in the LPFG is at an acceptable magnitude. To do so the uncertainty in sensitivity is chosen to be 5% of the value of the sensitivity.

Additional values used:

Table 7.4: Summary of Mandrel uncertainties

Variable	Value	Uncertainty	$\frac{\sigma_z}{z}$
$\frac{d\lambda_D}{d\epsilon}$	1980 $nm/m\epsilon$	99 $nm/m\epsilon$	5×10^{-2}
E_f	2.8×10^9 Pa	0.2×10^9 Pa	7.14×10^{-2}
μ_m	4.9×10^{-1}	0.1×10^{-1}	2.04×10^{-2}
E	24×10^6 Pa	0.5×10^6 Pa	2.08×10^{-2}
ρ	1200 kg/m^3	5 kg/m^3	4.16×10^{-3}

Where E_f is Young's Modulus of the fibre, μ_m is the Poisson Ratio of the mandrel, E is the Young's Modulus of the mandrel, and ρ is the density of the mandrel. Tolerances in the radius and length of the mandrel are neglected, as their impact on the sensitivity of a LPFG is negligible.

The theoretical Poisson Ratio of Polyurethane is 0.5, but in uncertainty analysis this cannot be assumed. The uncertainty stated above is a reasonable estimate as discussed in Qi and Boyce

(2005). The uncertainty for ρ, is estimated to be within the last decimal place in the provided density of $1.20 g/cm^3$ (Roylance, 1999).

Resulting Uncertainties:

Table 7.5: Summary of Resultant Mandrel uncertainties

Variable	Value	Uncertainty	$\frac{\sigma_z}{z}$
X	1.07×10^{0}	6.58×10^{-2}	6.17×10^{-2}
K_{eff}	6.28×10^{5} Pa	3.34×10^{4} Pa	5.33×10^{-2}
$\left(\frac{\delta\lambda_D}{a_0}\right)_0$	-4.62×10^{-11}	4.52×10^{-12}	9.79×10^{-2}

Considering tolerances in some of the mandrel's components were up to 7%, the final uncertainty in the sensitivity of the mandrel is less than 10%. This implies that there were no new significant concerns in the uncertainty of the mandrel, other than the LPFG sensitivity.

Polyurethane mandrel is considered to be in a quasi-static stress state, and the uncertainties concerning the various Young's Moduli and Poisson Ratios used in this calculation are likely greatly overstated, since these values are experimentally derived by applying much greater stains on the materials in comparison to what is considered here. For this reason it is reasonable to conclude that uncertainty contributions to the system, which stem from the fibre's and the mandrel's mechanical properties, are negligible, and only the uncertainty in the LPFG's sensitivity and κ are important. Section 7.2 tackles the problem of exactly how much precision is required in making a fibre, such that the sensitivity discussed in this thesis can be achieved.

7.2 Required Tolerance values for reproducible LPFG

7.2.1 Introduction

In the previous section, a significant problem was identified with the proposed LPFG design, namely unacceptable uncertainties concerning the sensitivity and mode coupling coefficient. These uncertainties were attributed to the tolerances of initial constants that define the geometry fibre. Working backwards from a desired strain sensitivity uncertainty, the tolerances in the variables describing the fibre required in order to achieve said sensitivity uncertainty can be calculated. Doing this has the added implication that all variables describing the fibre contribute equally to the uncertainty in LPFG sensitivity, as having any one variable with high tolerance would cause it to dominate the uncertainty of any variable it is a function of. It follows that, by extending on the work of Bevington and Robinson (2003, Chapter 4) discussed in the previous chapter, the required uncertainty for each dependant variable σ_{v_j} is:

$$\sigma_{v_j} = \frac{\sigma_z}{\sqrt{j_{\text{total}}}} \left(\frac{\partial z}{\partial v_j} \right)^{-1}, \tag{7.3}$$

where σ_{v_j} is the required standard deviation of each variable v_j, σ_z is the desired standard deviation in function z, v_j is the j^{th} dependant variable of z and j_{total} is number of independent variables v_j that define z.

Discussed here is how precise of measurement in each of these variables needs to be in order to achieve a 5% uncertainty in the LPFG sensitivity across a range of sensitivities: 2000 nm/mϵ, 200 nm/mϵ, 20 nm/mϵ, and 2 nm/mϵ. Additionally, investigated here is the effect on the required precision in these same variables due to also requiring 5% uncertainty in achieving ideal LPFG absorption bandwidth, i.e. 5% uncertainty in κ.

7.2.2 Derivation of Uncertainties

Solving the uncertainty in the LPFG strain sensitivity highlights that it is possible to work backwards and find what tolerances in the initial constants are required in order to achieve a desired uncertainty in the sensitivity and/or κ. This is done in such a way that no initial constant dominates final uncertainty of 5% in $\frac{d\lambda_D}{d\epsilon}$ or κ. As stated, the experimental implication of this is that a reduction in some but not all, initial constant tolerances which are calculated here, will not be effective in improving the sensitivity uncertainty. In other words, all variable's tolerance requirements need to be met such that the desired uncertainty can be achieved.

To get an understanding of how required tolerances change with different sensitivity requirements, minimum initial constants' tolerances are calculated for sensitivities of: 2000 nm/mϵ; 200 nm/mϵ; 20 nm/mϵ; and 2 nm/mϵ. Also, uncertainty requirements for κ become relevant as required sensitivity drops. Both of these cases are looked, firstly where only sensitivity uncertainty is important, and secondly where the uncertainty in κ is also considered. In the latter case, the evaluation in LPFGuncertainty.nb aims to bring uncertainty of κ to a value where its gives sufficient knowledge of the maximum refractive index, σ, such that it is comparable to the real uncertainty in σ of about 5%, as discussed in Section 7.1.2.

Table 7.6: Required tolerances in initial constants for 2000, 200, 20, 2 nm/mϵ, where uncertainty in κ is neglected, expressed as $\frac{\sigma_z}{z}$

Variable	2000 nm/mϵ	200 nm/mϵ	20 nm/mϵ	2 nm/mϵ
a_1	3.35×10^{-5}	3.35×10^{-4}	3.35×10^{-3}	3.35×10^{-2}
a_2	5.71×10^{-6}	5.71×10^{-5}	5.71×10^{-4}	5.71×10^{-3}
n_1	5.08×10^{-9}	5.08×10^{-8}	5.08×10^{-7}	5.08×10^{-6}
n_2	5.22×10^{-9}	5.22×10^{-8}	5.22×10^{-7}	5.22×10^{-6}
μ	5.02×10^{-5}	5.02×10^{-5}	5.02×10^{-5}	5.02×10^{-5}
p_{11}	1.00×10^{-4}	1.00×10^{-4}	1.00×10^{-4}	1.00×10^{-4}
p_{12}	5.32×10^{-5}	5.32×10^{-5}	5.32×10^{-5}	5.32×10^{-5}
Λ	3.39×10^{-6}	3.39×10^{-5}	3.39×10^{-4}	3.39×10^{-3}

Table 7.6 illustrates that decreases in desired strain uncertainty create proportional decreases in the required minimum tolerance of most of the variables. However tolerance requirements in μ, p_{11}, and p_{12} (which define the elasto-optic properties of the fibre) do not decrease, because their required tolerance is a function of the desired strain sensitivity uncertainty as well as γ (Eq. 3.58), both of which drop proportionately at each desired strain tolerance. In other words when considering Eq. 7.3, where $z = \frac{d\lambda_D}{d\epsilon}$ (Eq. 3.56) and $j = \mu, p_{11}, \text{or} p_{12}$, it can be shown that a reduction in σ_z are offset by equal falls in $\frac{\partial z}{\partial v_j}$ due to the inverse relationship.

Typically these variables are considered constants for a material, and may not change drastically over the length of a single LPFG or a series of LPFGs, however precise knowledge in their value is

important in designing a LPFG. It may be beneficial to experimentally derive more precise values for these constants in order to accurately model a LPFG, as their tolerance is not critical to the reproducibility of fibre manufacture.

Interestingly, at sensitivities around 2 and 20 nm/mϵ, some of the required tolerances are close to the initial vales used in Section 7.1. Many reported strain sensitivities in LPFGs (Shu et al., 2002; Wang et al., 2006; Zhao et al., 2008) fall in this range, which may correspond to a limit imposed by the tolerances in the LPFG periodicity, Λ, and the radii of the core and cladding, a_1 and a_2.

When considering κ, to have knowledge of the absorption spectrum, the minimum tolerance do not change unless a very high sensitivity is required. In Table 7.7 certainty in κ is considered to be within at 5%:

Table 7.7: Required tolerances in initial constants for 2000, 200, 20, 2 nm/mϵ, where uncertainty in κ is not neglected, expressed as $\frac{\sigma_z}{z}$

Variable	2000 nm/mϵ	200 nm/mϵ	20 nm/mϵ	2 nm/mϵ
a_1	3.35×10^{-5}	1.60×10^{-4}	1.58×10^{-4}	1.40×10^{-4}
a_2	5.71×10^{-6}	1.03×10^{-5}	1.02×10^{-5}	9.04×10^{-6}
n_1	5.08×10^{-9}	5.08×10^{-8}	5.08×10^{-7}	5.36×10^{-7}
n_2	5.22×10^{-9}	2.63×10^{-8}	2.59×10^{-8}	2.29×10^{-8}
μ	5.02×10^{-5}	5.02×10^{-5}	5.02×10^{-5}	5.02×10^{-5}
p_{11}	1.00×10^{-4}	1.00×10^{-4}	1.00×10^{-4}	1.00×10^{-4}
p_{12}	5.32×10^{-5}	5.32×10^{-5}	5.32×10^{-5}	5.32×10^{-5}
Λ	3.39×10^{-6}	3.39×10^{-5}	3.39×10^{-4}	3.39×10^{-3}

When ideal absorption spectrum bandwidth is important for the LPFG, primarily when one needs to know how to design a heterodyne for the LPFG, tolerance requirements are difficult to overcome even at lower desired sensitivities, as illustrated in Table 7.7. At high sensitivities, uncertainty requirements in sensitivity dominate, as the first columns in both Table 7.6and Table 7.7 are the same.

It is clear from this uncertainty analysis, that tolerance in fibre characteristics has a huge impact on the function of a LPFG. The difference between fibres being manufactured today and fibres needed to create highly sensitive, narrow bandwidth LPFGs, which can be utilised as hydrophones, is on the order of several orders of magnitude. Regardless, low sensitivity, large dynamic range LPFGs should be feasible, and useful for down-hole depth sensors. This kind of uncertainty analysis should ideally be applied to analyse the usefulness of every other interferometric or frequency-domain method conceived in the future, assuming it has a sufficiently robust mathematical model, as it is faster and cheaper than experimental work.

7.3 Conclusion

The uncertainty analysis has shown that a highly sensitive LPFG build around the concept of a VLAD discussed in Chapter 6 is difficult to produce with the single-mode optic fibres considered here, but it is important to keep in mind that other fibre options exist, specifically Photonic Crystal Fibre (PCF) which is currently a hot topic of research in LPFG design. Moreover a Down-Hole

instrument is still feasible as in such scenarios sensitivity does not need to be high, only the dynamic range needs to be broad enough to cope with the high down-hole pressures.

Chapter 8

Down-Hole Implementation and Future Work

8.1 Down-Hole Implementation

While Section 7.2 has shown that utilising the LPFG as a hydrophone is a task that is presently likely unachievable, the analysis did manage to show that reliably making LPFGs of lower sensitivity is something that can be accomplished with current commercial products. This means that LPFGs for Down-Hole applications are something that can be immediately possible. However, many of the methods outlined in Chapter 2 are useful in this implementation. The main benefit of these methods is that the dynamic range is only limited by the bandwidth which the sensitivity can sweep across, and that combined with short required lengths of fibre allows for easy down-hole implementation. One issue that will plague all of these methods is that in Down-Hole scenarios, high temperatures also create frequency shifts.

For LPFGs, work by Zhao et al. (2008) investigates a case where a strain-sensitive LPFG inscribed into Photonic Crystal Fibre (PCF), is insensitive to temperature changes. They accomplished this by solving the work of Shu et al. (2002) for modes where the thermo-optic effects (ξ_{co} and ξ_{cl}) cancel out the thermal expansion (α) of the fibre, as per the following:

$$\frac{d\lambda}{dT} = \gamma\lambda\left(\alpha + \frac{\xi_{\text{co}} n_{\text{effco}} - \xi_{\text{cl}} n_{\text{effcl}}}{n_{\text{effco}} - n_{\text{effcl}}}\right) \tag{8.1}$$

Maintaining a low but modest strain sensitivity of 2.68 nm/mϵ in experimental confirmation of their theory, they showed temperature sensitivity as low as 0.007 nm/°C. Their work used PCF which has been a focus of much recent research especially with LPFGs as these fibres are specifically designed to be able to control the modes propagating through them, and also have naturally very low ξ_{co} and ξ_{cl}. This is a complicating factor, as typically PCF is made from silicon, and would not be able to be wound in a sufficiently tight radius, so achieving similar results in a plastic fibre considered here would rely on using a type of plastic PCF, depending on the fibre's thermo-optic coefficients, as well as carefully resolving the tight bending effects. Solving Eq. 8.1 for zero sensitivity is an exercise not too dissimilar to the analysis for finding high sensitivity modes, and would require equally rigorous uncertainty analysis.

Other than LPFGs, there are publications of other temperature insensitive OFDR methods. In a paper by Martins et al. (2011) Fibre Bragg Gratings (FBG) were utilised as mirrors that shift spectra created by both Raman shifted and Rayleigh scattered light, creating roughly double the sensitivity compared to a single FBG, i.e. 2.35 nm/mϵ. Their arrangement, looks at the difference in wavelength between two FBGs tuned to act as mirrors to the Rayleigh and Raman pumps, where they have the same shift to temperature but opposing wavelength shifts to the strain. Thus they effectively achieved double the strain sensitivity compared to a single FBG, and negated any temperature variations.

Tapered Rayleigh scattering also shows great promise as a temperature insensitive sensor. Wang et al. (2012b) investigates the temperature dependence of a tapered fibre, managing to show a temperature sensitivity of 0.1 nm/°C and an impressive strain sensitivity of 17.17 nm/mϵ. However, such a high sensitivity may be too high for a Down-Hole instrument. Additionally tapered fibres are quite fragile, and use as a Down-Hole instrument, especially whilst drilling, is likely to damage them.

Other methods are intrinsically sensitive to temperature, thus sensing only strain and not temperature is not possible. For example, temperature dependence of Brillouin backscattering in a range of doped fibres was investigated by Mizuno et al. (2012) as well Brown et al. (2005), and illustrated that while frequency shift per unit temperature ($^{\circ}C$) was up to 50 times less than the frequency shift per unit strain ($m\epsilon$), there was no way to eliminate temperature shifts entirely, which would be a significant issue in high temperature and high pressure environments, unless there was a separate temperature instrument with which to correct against.

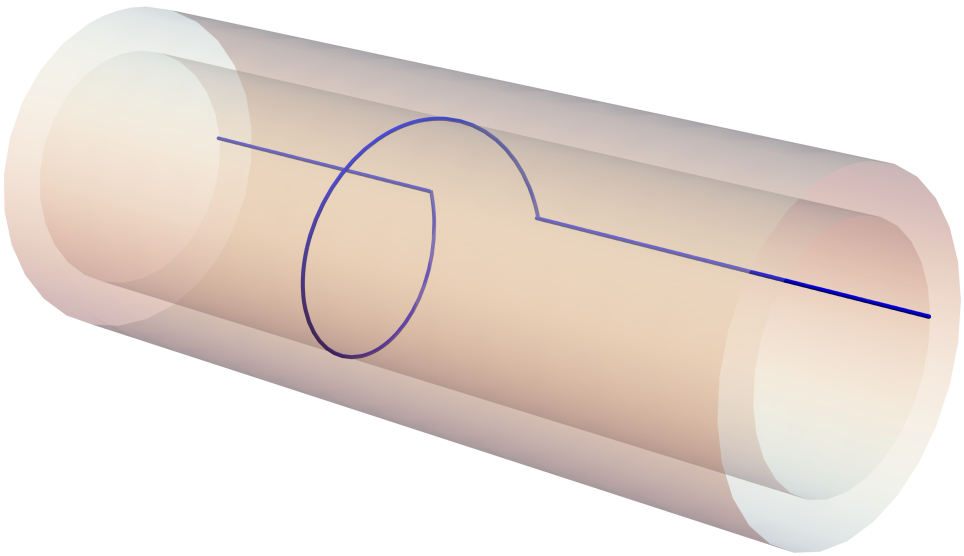

Figure 8.1: Illustration of how a LPFG, or other OFDR sensor, could be implemented into a Coiled Tube section, to act as a depth or acoustic sensor

DET CRC is developing a Coiled Tubing drilling system (CT drilling). This particular drill has a hollow section in the middle where pressure sensors could be installed. Specifically, a fibre optic depth sensor could be installed near the drill bit, and/or pressure sensors for seismic while

drilling could also be arranged at intervals along the entire length of Coiled Tubing. A simple illustration of all that is needed for such a sensor is show in Figure 8.1. The loop could be any of the frequency-domain sensors discussed, and simply needs to be adhered to the inside wall of the Coiled Tubing to be able to couple to external pressure changes.

8.2 Future Work

There is a range of opportunities for future work that have been highlighted so far. Here is a summary of specific topics that are deemed worthy of detailed research due to exhibiting qualities that make them appropriate for use in down-hole or hydrophone sensors.

8.2.1 Down-hole

When considering a down-hole instrument, there are several avenues where this research can continue. The first potential topic of interest is the theoretical evaluation of temperature insensitive LPFG. Such LPFGs are expected to have solutions for a range of laser wavelengths, likely giving some control over what sensitivity and absorption bandwidth can achieved with a chosen mode. Having narrower bandwidth with less sensitivity will make it much easier for a heterodyne arrangement to function to higher Down-Hole pressures without modifying the AOM frequency and heterodyne intermediate filter. Also worth considering are PCF fibres as PCFs have been shown to be generally insensitive to temperature (Dobb et al., 2004).

Another good topic would be experimental work extending on the work of Martins et al. (2011) for FBG based tools. This tool exhibited impressive linear sensitivity to strain in the wavelength domain, and with some modifications to the sensing mechanism to allow for higher dynamic range would warrant significant attention. Such a tool would not need to have a broadband source, however the detectors would still need to be broadband due to resolving the shifts in wavelengths due to strain across a desired dynamic range.

In the hydrophone scenario, Brillouin backscattering was quickly dismissed due to its poor sensitivity characteristics. However Down-Hole, its narrow bandwidth and lower sensitivity to strain make it a fantastic spectroscopic tool in very high pressure (and hence high strain) environments. Additionally, the nature of Brillouin backscattering means that the requirement for a broadband source is negated, and modern stable frequency lasers should be used, as that improves the definition of the Brillouin frequency.

8.2.2 Hydrophones

Much of this thesis has focussed on the viability of frequency-domain sensing methods implemented into hydrophones. The single biggest challenge was to find a method exhibiting very high strain sensitivity. The LPFG has been discussed at some length, concluding that the precision of optical fibre required to have confidence in the cladding modes was not available with commercially advertised fibres. To further this work, very precisely manufactured and well understood fibre will be needed, or even research with a plastic variety of PCF.

A topic not deeply explored is the strain sensitivities of bent, tapered Rayleigh backscattering. As discussed in Section 2.2.3.3, this arrangement exhibited extreme sensitivity to external refractive

index change. With experimental research into strain sensitivity of Tapered sections using Rayleigh backscattering bent (or wrapped) around a mandrel, a very sensitive frequency domain sensor could be feasible, using a DBR laser to allow fast sweeps across wavelengths.

Other than that it is unlikely that fibre only frequency domain sensors will be possible, and incorporating crystals into the system would open up wide array of options, especially in Raman spectroscopy or even more modern concepts. There are other avenues such as in monitoring shifts in excitation transitions of electron-photon emissions. In quantum bit storage research by Robledo et al. (2011), the quantum spin state of electrons around a defect in a diamond is read from the florescence due to the decay of optical excitation transitions in the electrons. Their work is plagued by minute stresses on the diamond crystal which causes spectral line broadening of these emissions. This can be utilised to instead monitor the stress state of the crystal using a self-heterodyne (Okoshi et al., 1980). After-all, one man's noise is another man's signal.

Chapter 9

Conclusions

The main goal of the Thesis was to consider the somewhat novel approach of implementing frequency-domain shifts due to strains on an optic fibre to construct pressure sensors which can be implemented into a range of geophysical contexts. Frequency-domain sensors are not widely considered in literature due to an inherent difficulty in achieving good sensitivity with these approaches. Consequently, the first step in considering such designs was to find a fibre optic implementation that is frequency sensitive to strains on the fibre. This highlighted Long Period Fibre Gratings (LPFGs) as one of the most sensitive solutions to this major hurdle. This was due to the gratings having well understood mechanics, high linear theoretical strain sensitivity, and potentially low temperature sensitivity. Bent-tapered Rayleigh backscattering mechanism also was identified as having very high strain sensitivity, however due to the mechanism's still poorly understood theory it was not possible to analyse in a way similar to how the LPFG is analysed.

Long Period Fibre Gratings are considered in the context of winding them around a small compliant mandrel, in order to make the most out of the fact that LPFGs require significantly less active fibre than traditional phase-domain windings. This requires the use of a variety of plastic fibre which can be tightly wound, which raises issues of fibre birefringence. This issue can be resolved by polarizing the light entering the wound LPFG such that the birefringence effects are minimised. Assuming these issues can be experimentally overcome, small compliant mandrels are shown to have good sensitivity characteristics and the uncertainty analysis for them indicates that their fabrication is not a major concern for the operation of the sensor.

Since the intention is that sensing is made in the frequency-domain, a simple heterodyne arrangement is a good way to interrogate the signal with good signal to noise ratio. The wide bandwidth of the LPFG notch is a problem but the combined strength of the source and signal arms should be enough to overcome a requirement for a fairly broad intermediate filter. If this is an issue experimentally, a solution to this is likely to use an intermediate filter which is restricted to look at only one slope of the absorption curve; or to have a much longer LPFG and deal with only one of many much narrower signal bands.

Regardless, uncertainty analysis performed on highly sensitive LPFGs reveals that the tolerances in manufacture of step-index single-mode fibres are much too big to be able to reproducibly create such gratings. A hot topic of LPFG research is Photonic Crystal Fibres (PCFs), which have superior modal dispersion properties compared to traditional fibres used in telecommunication

scenarios. As this is likely to make LPFGs significantly easier to produce, future research into instrumentation should try to focus on such fibres. Even though the fibres studied here will have problems performing in a high sensitivity scenario, down-hole sensors would not have such an issue. Since LPFGs operate in the frequency-domain, the nature of the observed signal lends itself nicely to down-hole use, since their dynamic range is so broad that a down-hole sensor could operate across a wide range of pressures.

Overall, frequency-domain strain sensors have very real potential for implementation as pressure sensors, maybe not yet as hydrophones, but definitely as down-hole pressure sensors. It is important to go on to do further theoretical and experimental research into several thermally insensitive mechanisms that would make good down-hole sensors.

Acknowledgements

Lastly I would like to extend my gratitude to a multitude of people that have had an impact, on me finishing this thesis.

Foremost, I express my sincere gratitude to my supervisor Associate Professor Anton Kepic. Anton was not only my guide in my thesis but he was instrumental in me receiving scholarship from the Deep Exploration Technologies CRC (DET CRC), without which I would not have come even remotely close to finishing this thesis. With that said, I appreciate the contribution of all members of the DET CRC, and our project leader Associate Professor Brett Harris. The work has been supported by the Deep Exploration Technologies Cooperative Research Centre whose activities are funded by the Australian Governments Cooperative Research Centre Programme. This is DET CRC Document 2015/755.

Thanks also extend to the anonymous examiners for their constructive criticisms and highlighting of conceptual misunderstandings and mistakes. I have done my best to address all their highlighted concerns in order to improve the quality of this body of work.

A special mention goes out to my old Professor, now Adelaide University's Director for Experimental Physics: Andre Luiten. Before even committing to do my Master's thesis his comments helped me decide on pursuing further academic studies, and I look forward to crossing paths with him again in the future.

Within the Department of Exploration Geophysics, I wish to extend appreciation to Associate Professor Maxim Lebedev, who cheerfully interviewed me and took me on as a student in the department.

For help with editing my thesis I obviously have my supervisor to thank for taking the time to critique my work, but also my mother, Albena Bossilkova, for also going through and correcting the slew of grammatical errors and unfinished sentences that I had failed to notice myself.

I have formed many great bonds with the students here, namely: Muhammad Shahadat Hossain, Mohammed Al Hosni, Mohammad J Khoshnavaz, Pouya Ahmadi, Ida Hooshyari Far, and particularly Mateus Meira. You have all in your own little ways made being a poor lowly Master's student life bearable, I thank you all for your kind words, and wish you all the very best in your own theses.

The fact that so many my fellow students from the University of Western Australia went on to become doctors of various types has in some way motivated me to start following in similar footsteps. There are too many to name individually, most of whom now live overseas doing exciting things that I am jealous of.

And thank you to my mum and dad, for their general support and their occasional free food. Who knows how much skinnier I would be without the free food.

Of course, thank you also goes to my partner Natasha Muller. Mostly for putting up with me all this time, and also keeping us alive through means of patching our financial issues by spending most nights working rather than being out with her friends. With this thesis done, I hope to devote more time to you.

Appendix A

LPFG in fibres with refractive index and diameter modulation

Whilst UV induced refractive index changes in LPFG inscribed optic fibre are a popular method of inscribing said LPFG, that is by no means the only way to inscribe a LPFG. Electric arc discharge or CO_2 lasers can be used to create diameter and refractive index contrast, and changes the way the LPFG is theoretically evaluated.

Palma-Quiroz et al. (2008) illustrates the mathematical model used to cope with these methods as the calculation for the coupling constant κ (see Eq. 3.42) changes significantly. The evaluation of κ is split into the sum of the contributions of refractive and radius perturbations.

Refractive index Changes are treated a similar way as in Eq. 3.54:

$$n_i(z) = n_i\left(1+\sigma_i\left(1+\cos\left(\frac{2\pi}{\Lambda}z\right)\right)\right), \tag{A.1}$$

where σ is the refractive index modulation profile, and i denotes the layer ($i=1$ refers to the core and $i=2$ refers to the cladding). Similarly radial changes are of the following form:

$$a_i(z) = a_i\left(1+\rho_i\left(1+\cos\left(\frac{2\pi}{\Lambda}z\right)\right)\right), \tag{A.2}$$

where ρ is the radial modulation profile. Using these the full evaluation of κ becomes:

$$\begin{aligned}\kappa = &\sum_{i=1}^{2}\frac{\omega\epsilon_0 n_i(z)^2\alpha_i}{4}\int_0^{2\pi}\int_{a_{i-1}}^{a_i}\left(E_r^{\mathrm{cl}}\left(E_r^{\mathrm{co}}\right)^* + E_\phi^{\mathrm{cl}}\left(E_\phi^{\mathrm{co}}\right)^*\right)rdrd\phi \\ &+\sum_{i=1}^{2}\frac{\omega\epsilon_0\left(n_i(z)^2 - n_{i+1}(,z)^2\right)}{8}\int_0^{2\pi}\int_{a_{i-1}(1+\rho_i)}^{a_i(1+2\rho_i)}\left(E_r^{\mathrm{cl}}\left(E_r^{\mathrm{co}}\right)^* + E_\phi^{\mathrm{cl}}\left(E_\phi^{\mathrm{co}}\right)^*\right)rdrd\phi\end{aligned} \tag{A.3}$$

In this equation E_r^{cl} and E_ϕ^{cl} have different functional forms for $r \le a_1$ and $a_1 \le r \le a_2$. In the cases of $r \le a_1$:

$$E_r^{\mathrm{cl}} = \mathbb{i}E_{1\nu}{}^{\mathrm{cl}}\frac{u_1}{2}\left(J_2(u_1r) + J_0(u_1r) - \frac{\sigma_2\zeta_0}{{n_1}^2}\left(J_2(u_1r) - J_0(u_1r)\right)\right)e^{\mathbb{i}\phi}e^{\mathbb{i}\left({\beta_1}^{\mathrm{co}}z-\omega t\right)} \tag{A.4}$$

$$E_{\phi}^{\mathrm{cl}} = {E_{1\nu}}^{\mathrm{cl}} \frac{u_1}{2} \left(J_2\left(u_1 r\right) - J_0\left(u_1 r\right) - \frac{\sigma_2 \zeta_0}{{n_1}^2} \left(J_2\left(u_1 r\right) + J_0\left(u_1 r\right) \right) \right) e^{\mathbb{i}\phi} e^{\mathbb{i}\left({\beta_1}^{\mathrm{co}} z - \omega t\right)} \tag{A.5}$$

And in the cases of $a_1 \leq r \leq a_2$:

$$E_r^{\mathrm{cl}} = \mathbb{i} {E_{1\nu}}^{\mathrm{cl}} \frac{\pi a_1 u_1^2 J_1\left(u_1 a_1\right)}{2} \left(-\frac{F_2}{r} p_l(r) + \frac{1}{u_2 r} q_l(r) - \frac{\sigma_2}{{n_2}^2} \left(u_2 G_2 r_l(r) - \frac{{n_2}^2 \zeta_0}{{n_1}^2} s_l(r) \right) \right) e^{\mathbb{i}\phi + \mathbb{i}\left({\beta_1}^{\mathrm{co}} z - \omega t\right)} \tag{A.6}$$

$$E_{\phi}^{\mathrm{cl}} = {E_{1\nu}}^{\mathrm{cl}} \frac{\pi a_1 {u_1}^2 J_1\left(u_1 a_1\right)}{2} \left(\frac{\sigma_2}{{n_2}^2} \left(\frac{G_2}{r} p_l(r) + \frac{{n_2}^2 \zeta_0}{{n_1}^2 u_2 r} q_l(r) \right) + u_2 F_2 r_l(r) - s_l(r) \right) e^{\mathbb{i}\phi + \mathbb{i}\left({\beta_1}^{\mathrm{co}} z - \omega t\right)} \tag{A.7}$$

This evaluation of κ will be needed for correct modelling of LPFGs with inscriptions that alter the fibre radius. However the uncertainty analysis significantly more difficult, as uncertainties in the repeatability of the radial inscription profile discussed in Yin et al. (2014) need to be accounted for.

Bibliography

Adachi, S. (2005). *Properties of Group-IV, IIIV and IIVI Semiconductors*. John Wiley & Sons Ltd.

Allsop, T., Gillooly, A., Mezentsev, V., Earthgrowl-Gould, T., Neal, R., Webb, D. J., and Bennion, I. (2004). Bending and orientational characteristics of long period gratings written in d-shaped optical fiber. *IEEE Transactions on Instrumentation and Measurement*, 53:130.

Bevington, P. and Robinson, D. (2003). *Data reduction and error analysis for the physical sciences 3rd edition*. New York, NY: McGraw-Hill.

Bingham, S. J., Brger, B., Suter, D., and Thomson, A. J. (1998). The design and sensitivity of microwave frequency optical heterodyne receivers. *Review of Scientific Instruments*, 69:3403–3409.

Block, U. L., Dangui, V., Digonnet, M. J. F., and Fejer, M. M. (2006). Origin of apparent resonance mode splitting in bent long-period fiber gratings. *Journal of Lightwave Technology*, 24:1027.

Boyd, R. (2008). *Nonlinear Optics*. Burlington, MA: Academic Press.

Brown, K., Brown, A. W., and Colpitts, B. G. (2005). Characterization of optical fibers for optimization of a brillouin scattering based fiber optic sensor. *Optical Fiber Technology*, 11:131–145.

Callsen, G., Reparaz, J. S., Wagner, M. R., Kirste, R.and Nenstiel, C., Hoffmann, A., and Phillips, M. R. (2011). Phonon deformation potentials in wurtzite gan and zno determined by uniaxial pressure dependent raman measurements. *Applied Physics Letters*, 98:061906.

Chen, D., Liu, W., Jiang, M., and He, S. (2009). High-resolution strain/temperature sensing system based on a high-finesse fiber cavity and time-domain wavelength demodulation. *Journal of Lightwave Technology*, 24:1027.

Chiavaioli, F., Trono, C., and Baldini, F. (2013). Specially designed long period grating with internal geometric bending for enhanced refractive index sensitivity. *Applied Physics Letters*, 102:231109.

Chung, K. M., Dong, L., Lu, C., and Tam, H. (2011). Novel fiber bragg grating fabrication system for long gratings with independent apodization and with local phase and wavelength control. *Optics Express*, 19:12664.

Das, R. and Agrawal, Y. (2011). Raman spectroscopy: Recent advancements, techniques and applications. *Vibrational Spectroscopy*, 57:163–176.

Ding, Z., Yao, X. S., Liu, T., Du, Y., Liu, K., Han, Q., Meng, Z., and Chen, H. (2012). Long-range vibration sensor based on correlation analysis of optical frequency-domain reflectometry signals. *Optics Express*, 20:28319.

Dobb, H., Kalli, K., and Webb, D. (2004). Temperature-insensitive long period grating sensors in photonic crystal fibre. *Electronics Letters*, 40:657–658.

Draka (2010). Drakaelite, bendbright - elite fiber for patch cord. Draka, a brand of the Prysmian Group.

Dudley, J. M. and Taylor, J. R., editors (2010). *Supercontinuum Generation in Optical Fibers*. Cambridge, UK: Cambridge University Press.

Erdogan, T. (1997a). Cladding-mode resonances in short- and long- period fiber grating filters. *Journal of the Optical Society of America*, 14:1762.

Erdogan, T. (1997b). Fiber grating spectra. *Journal of Lightwave Technology*, 15:1277.

Fielding, A. J., Edinger, K., and Davis, C. (1999). Experimental observation of mode evolution in single-mode tapered optical fibers. *Journal of Lightwave Technology*, 17:1649.

Forrester, A. (1961). Photoelectric mixing as a spectroscopic tool. *JOSA*, 51:253–256.

Froggatt, M. and Moore, J. (1998). High-spatial-resolution distributed strain measurement in optical fiber with rayleigh scatter. *Applied Optics*, 37:1735.

Galeener, F. L., Mikkelsen, J. C., Geils, R. H., and Mosby, W. J. (1987). The relative raman cross sections of vitreous sio2, geo2, b2o3, and p2o5. *Applied Physics Letters*, 32:34–36.

Gonzalez, D. A.alez, D. A., Arce-Diego, J. L., Cobo, A., and Lopez-Higuera, J. M. (2001). Spectral modelling of curved long-period fibre gratings. *Measurement Science and Technology*, 12:786–792.

Grattan, K. and Sun, T. (2000). Fiber optic sensor technology: an overview. *Sensors and Actuators*, 82:40–61.

Han, M., Wang, Y., and Wang, A. (2007). Grating-assisted polarization optical time-domain reflectometry for distributed fiber-optic sensing. *Optics Letters*, 32:2028.

Hirai, A. (2001). New broad-spectrum interferometry for high-sensitive measurement. *The 4th Pacific Rim Conference on, Lasers and Electro-Optics, 2001. CLEO/Pacific Rim 2001.*, 1:I–468.

Hui, X., Zhou, J., Xu, C., Zheng, S., Chi, H., Jin, X., and Zhang, X. (2013). A real-time detection and self-control phase-sensitive otdr distributed sensor system. In *2013 12th International Conference on Optical Communications and Networks (ICOCN)*, page 1. DOI: 10.1109/ICOCN.2013.6617198.

James, S. and Tatam, R. (2003). Optical fibre long-period grating sensors: characteristics and application. *Measurement Science and Technology*, 14:R49–R62.

Kim, B., Ahn, T., Kim, D., Lee, B., Y., C., Paek, U., and Han, W. (2002). Effect of co2 laser irradiation on the refractive-index change in optical fibers. *Applied Optics*, 41:3809.

Leonard, J. and Cimini, J. (1989). Optical phase division multiplexing for local communications applications. *IEEE Transactions on Communications*, 37:1282.

Lin, H., Mokhtara, M., Rahmanb, F., Abdul Rashida, H., Roslinac, M., and Arif, N. (2012). Simultaneous spectral recovery of long-period grating sensor array using optical time-division multiplexing. *Optick*, 123:650–652.

Lu, B., Pan, W., Zou, X., Yan, X., Yan, L., and Luo, B. (2015). Wideband doppler frequency shift measurement and direction ambiguity resolution using optical frequency shift and optical heterodyning. *Optics Letters*, 40(10):2321.

Lu, Y., Zhu, T., Chen, L., and Bao, X. (2010). Distributed vibration sensor based on coherent detection of phase-otdr. *Journal of Lightwave Technology*, 28:3243.

Martins, H., Marques, M., and Frazo, O. (2011). Temperature-insensitive strain sensor based on four-wave mixing using raman fiber bragg grating laser sensor with cooperative rayleigh scattering. *Applied Physics B: Lasers and Optics*, 104:957–960.

Matsumoto, H. and Hirai, A. (1999). A white-light interferometer using a lamp source and heterodyne detection with acousto-optic modulators. *Optics Communications*, 170:217–220.

Measures, R. M. (2001). *Structural monitoring with fiber optic technology*. San Diego, California: London : Academic.

Mises, v. R. (1945). On saint-venant's principle. *Bulletin of the American Mathematical Society*, 54:555–562.

Mizuno, Y., Hayashi, N., and Nakamura, K. (2012). Dependences of brillouin frequency shift on strain and temperaturein optical fibers doped with rare-earth ions. *Journal of Applied Physics*, 112:043109.

Mizuno, Y., He, Z., and Hotete, K. (2010). Distributed strain measurement using a tellurite glass fiber with brillouin optical correlation-domain reflectometry. *Optics Communications*, 283:24382441.

Morkel, P., Cowle, G., and Payne, D. (1990). Travelling-wave erbium fibre ring laser with 60 khz linewidth. *Electronics Letters*, 26:632 – 634.

Murphy, K. A., Gunther, M. F., Vengsarkar, A. M., and O., C. R. (1991). Quadrature phase-shifted, extrinsic fabry-perot optical fiber sensors. *Optics Letters*, 16:273.

Okoshi, T., Kikuchi, K., and Nakayama, A. (1980). Novel method for high resolution meansurement of laser ouput spectrm. *Electronics Letters*, 16:630.

Palma-Quiroz, I., Flores-Llamas, I., Osorio-Comparan, R., Khotiaintsev, S., and Svyryd, V. (2008). Modelling of long-period fiber gratings with both refractive index and diameter modulation. In *12th International Conference on Mathematical Methods in Electromagnetic Theory*.

Pechstedt, R. D. and Jackson, D. A. (1995). Design of a compliant-cylinder-type fiber-optic accelerometer: theory and experiment. *Applied Optics*, 34:3009.

Petrovic, J. (2008). *Modelling of Long Period Gratings in Photonic Crystal Fibres and Sensors Based on Them, Modelling and Simulation*. Rijeka, Croatia: InTech.

Piprek, J., editor (2005). *Optoelectronic Devices : Advanced Simulation and Analysis*. New York, NY : Springer New York.

Protopopov, V. V. (2009). *Laser Heterodyning*. Atlanta, GA: Springer-Verlag Berlin Heidelberg.

Qi, H. and Boyce, M. (2005). Stress-strain behavior of thermoplastic polyurethane. *Mechanics of Materials*, 37:817–839.

Qin, Z., Chen, L., and Bao, X. (2012). Wavelet denoising method for improving detection performance of distributed vibration sensor. *IEEE Photonics Technology Letters*, 24:542.

Raftopoulos, D. D., Karapanos, D., and Theocaris, P. S. (1976). Static and dynamic mechanical and optical behaviour of high polymers. *Journal of Physics D: Applied Physics*, 9:869.

Robledo, L., Childress, L., Bernien, H., Hensen, B., Alkemade, P. F. A., and Hanson, R. (2011). High-fidelity projective read-out of a solid-state spin quantum register. *Nature*, 477:574–578.

Rogers, A. J. (1981). Polarization-optical time domain reflectometry: a technique for the measurement of field distributions. *Applied Optics*, 20:1060.

Roylance, D. (1999). Mit open courseware: Mechanics of materials: Modules: Appendices: Material properties. Retrieved from http://ocw.mit.edu/courses/materials-science-and-engineering/3-11-mechanics-of-materials-fall-1999/modules/props.pdf.

Shajenko, P., Flatley, J. P., and Moffett, M. B. (1978). On fiber optic hydrophone sensitivity. *Journal of the Acoustical Society of America*, 64:1286.

Shen, F. and Wang, A. (2005). Frequency-estimation-based signal-processing algorithm for white-light optical fiber fabryperot interferometers. *Applied Optics*, 44:5207.

Shu, X., Zhang, L., and Bennion, I. (2002). Sensitivity characteristics of long-period fiber gratings. *Journal of Lightwave Technology*, 20:255.

Silva-Lpez, M., Fender, A., MacPherson, W. N., Barton, J. S., Jones, J. D. C., Zhao, D., Dobb, H., Webb, D. J., Zhang, L., and I., B. (2005). Strain and temperature sensitivity of a single-mode polymer optical fiber. *Optics Letters*, 30:3129.

Sugitatsu, A., Kawano, H., Hatta, T., and Kasahara, K. (2001). Novel fabrication technique of long period fiber gratings using a holographic optical element. *Optical Review*, 8:267–270.

Sun, L., Li, J., Tan, Y., Gao, S., Jin, L., and B., G. (2013). Bending effect on modal interference in a fiber taper and sensitivity enhancement for refractive index measurement. *Optics Express*, 21:26714.

Truong, G.-W., Anstie, J. D., May, E. F., Stace, T. M., and Luiten, A. N. (2012). Absolute absorption line-shape measurements at the shot-noise limit. *Physical Review A*, 86:030501.

Waagaard, O., Havsgrd, G., and G., W. (2001). An investigation of the pressure-to-acceleration responsivity ratio of fiber-optic mandrel hydrophones. *Journal of Lightwave Technology*, 19:994.

Wang, K., Wang, Q., Wang, Y., and Zhang, S. (2009). The use of long-period fiber grating bending sensing rules of the fiber-optic hydrophone. In *The Ninth International Conference on Electronic Measurement & Instruments*.

Wang, X., Li, W., Chen, L., and Bao, X. (2012a). Distributed mode coupling measurement along tapered single-mode fibers with optical frequency-domain reflectometry. *Journal of Lightwave Technology*, 30:1499.

Wang, X., Li, W., Chen, L., and Bao, X. (2012b). Thermal and mechanical properties of tapered single mode fiber measured by ofdr and its application for high-sensitivity force measurement. *Optics Express*, 20:14779.

Wang, Y., Wang, D. N., Jin, W., and Rao, Y. (2007). Asymmetric transverse-load characteristics and polarization dependence of long-period fiber gratings written by a focused co2 laser. *Applied Optics*, 46:3079.

Wang, Y., Wang, D. N., Wang, C., and Hu, T. (2013). Compressible fiber optic micro-fabry-prot cavity with ultra-high pressure sensitivity. *Optics Ex*, 21:14084.

Wang, Y., Xiao, L., Wang, D., and Jin, W. (2006). Highly sensitive long-period fiber-grating strain sensor with low temperature sensitivity. *Optics Letters*, 31:3414–3416.

Waxler, R. M., Horowitz, D., and Feldman, A. (1979). Optical and physical parameters of plexiglas 55 and lexan. *Applied Optics*, 18:101–104.

Welker, D. (2014). Paradigm Optics, The Polymer Division of INCOM Inc., 9600 NE 126th Avenue, Suite 2540, Vancouver, WA 98682. (Personal Communication).

Wood, D. (1994). *Optoelectronic Semiconductor Devices*. New York, NY: Prentice Hall.

Xiao, H., Deng, J., Pickrell, G., May, R. G., and Wang, A. (2003). Single-crystal sapphire fiber-based strain sensor for high-temperature applications. *Journal of Lightwave Technology*, 21:2276.

Xiao, L., Wang, D. N., and Jin, W. (2006). Highly sensitive long-period fiber-grating strain sensor with low temperature sensitivity. *Optics Letters*, 31:3414.

Ye, J. and Cundiff, S. T., editors (2005). *Femtosecond Optical Frequency Comb: Principle, Operation, and Applications*. Boston, MA: Springer US.

Yin, G., Wang, Y., Liao, C., Zhou, J., Zhong, X., Wang, G., Sun, B., and He, J. (2014). Long period fiber gratings inscribed by periodically tapering a fiber. *Photonics Technology Letters*, 26:698.

Yu, Q. and Zhou, X. (2011). Pressure sensor based on the fiber-optic extrinsic fabry-perot interferometer. *Photonic Sensors*, 1:72–83.

Yu, Francis To So & Yin, S. (2002). *Fiber Optic Sensors*. New York, NY: Marcel Dekker.

Zhang, Z. and Bao, X. (2008). Distributed optical fiber vibration sensor based on spectrum analysis of polarization-otdr system. *Optics Express*, 16:10240.

Zhao, C., Xiao, L., Ju, J., Demokan, M. S., and Jin, W. (2008). Strain and temperature characteristics of a long-period grating written in a photonic crystal fiber and its application as a temperature-insensitive strain sensor. *Journal of Lightwave Technology*, 26:220.

Zhu, N., Ke, J., Zhang, H., Chen, W., Liu, J., Zhao, L., and Wang, W. (2010). Wavelength coded optical time-domain reflectometry. *Journal of Lightwave Technology*, 28:972.